Università degli Studi di Padova

Dipartimento di Ingegneria dell'Informazione

Laurea Magistrale in Ingegneria delle Telecomunicazioni

Design of a fiber optic distributed acoustic sensor

Supervisor
Prof. Luca Palmieri

Master Candidate
Linda Brunelli

26 February 2018

Academic Year 2017/2018

Abstract

Distributed optical fiber sensors are a particular kind of sensors which use the whole fiber length for sensing purposes. Among them, Distributed Acoustic Sensors (DAS) can detect vibrations in a distributed way. DAS can be implemented with different techniques.
In this thesis, we have designed a distributed acoustic sensor based on a phase-sensitive OTDR (ϕ-OTDR), which exploits a highly coherent laser and the Rayleigh backscattered light to detect the perturbations. Both the acoustic wave frequency and the position of the perturbation along the fiber can be identified.
We have tested the performances of our experimental setup by acquiring the ϕ-OTDR traces and analyzing them both in the time and frequency domain.

Sommario

I SENSORI DISTRIBUITI IN FIBRA OTTICA utilizzano l'intera lunghezza della fibra come sensore. Tra di essi vi sono i sensori acustici distribuiti (DAS), che possono individuare eventuali vibrazioni in maniera distribuita. I DAS possono essere implementati secondo diverse tecniche.
In questa tesi è stato realizzato un sensore acustico distribuito basato su di un phase-sensitive OTDR (ϕ-OTDR), che sfrutta un laser ad alta coerenza e la luce retrodiffusa di Rayleigh per individuare le perturbazioni. Con questo metodo, è possibile individuare sia la frequenza dell'onda acustica, sia la posizione lungo la fibra in cui avviene la perturbazione.
Le prestazioni del setup sperimentale sono state testate attraverso l'acquisizione delle tracce del ϕ-OTDR e la loro analisi nel dominio del tempo e della frequenza.

Contents

Abstract **v**

List of figures **xii**

List of tables **xv**

1 Introduction **1**
- 1.1 Guide to Reading . . . 3

2 Theoretical background **5**
- 2.1 Rayleigh scattering . . . 5
- 2.2 OTDR . . . 7
- 2.3 Phase-sensitive OTDR . . . 12
- 2.4 ϕ-OTDR as a Distributed Acoustic Sensor . . . 14

3 Overview on Distributed Optical Fiber Sensors (DOFS) **15**
- 3.1 OTDR based sensors . . . 16
- 3.2 OFDR based sensors . . . 20

4 Experimental setup **23**
- 4.1 Light Source . . . 26
- 4.2 Erbium Doped Fiber Amplifier (EDFA) . . . 27
- 4.3 Acquisition board . . . 29
  - 4.3.1 Input parameters . . . 30
  - 4.3.2 Acquisition modes . . . 32
- 4.4 Setup parameters . . . 34
- 4.5 Data Analysis . . . 37

5 Results **39**
- 5.1 Preliminary analysis . . . 39
- 5.2 ϕ-OTDR traces . . . 40
- 5.3 Acoustic Sensing . . . 43

6 Conclusions **57**

References **59**

Listing of figures

1.1 Different kinds of fiber optic sensing [1]. 2

2.1 Attenuation in optical fibers. The solid line represents the measurement results, while the dotted lines are the theoretical limits due to Rayleigh scattering and molecular vibrations. 6
2.2 Schematic diagram of the spontaneous Rayleigh scattering process [2]. 7
2.3 Typical spontaneous scattering spectra. 7
2.4 Operating principle of an OTDR. 8
2.5 Example of an OTDR trace. 9
2.6 Minkowski diagram. 11
2.7 Simulated ϕ-OTDR trace [3]. 13

4.1 Scheme of the distributed acoustic sensor final setup. 24
4.2 Picture of the experimental setup. 26
4.3 Laser Koheras Adjustkit TAdE15PztSpM. 27
4.4 Output power comparison between FA-15 and FA-18. 28
4.5 EDFA gain. The solid line shows the theoretical limits, while the different markers represent different pump powers. 28
4.6 PDA14 board [4]. 29
4.7 Scheme of PDA14 functionality 31
4.8 Representation of the pulse period T_p and pulse width τ. 35
4.9 Scheme of a data matrix and its FFT. 37

5.1 Frequency analysis in three different conditions: only the photodiode is connected to the PDA14 (5.1a), the setup is completely connected but the laser is turned off (5.1b) and the FUT is not connected (5.1c). 41
5.2 ϕ-OTDR traces with different pulse widths. 42
5.3 LSA approximation of the trace to calculate the attenuation α. . 43
5.4 Spectrogram of the ϕ-OTDR when a perturbation with $f_a = 50$ Hz is applied. 44
5.5 3-D zoom on the FFT around the point of application of the perturbation. 45

5.6 Mean FFT around the perturbed portion of the fiber: comparison between reference and acoustic wave. 46
5.7 Normalized FFT when a perturbation of f_a=50 Hz is applied. . . 47
5.8 Normalized FFT around the acoustic wave position. 48
5.9 FFT of the filtered signal, averaged around the portion where the acoustic wave is applied. 49
5.10 Time domain visualization of the signal around the perturbation. 49
5.11 Spectrogram obtained by making the difference between each trace and the first one. 50
5.12 FFT obtained by making the difference between each trace and the first one around the perturbation. 51
5.13 Spectrogram of the traces when a perturbation with $f_a = 400$ Hz is applied. 53
5.14 Normalized spectrogram with respect to the average value when a perturbation with $f_a = 400$ Hz is applied. 54
5.15 FFT around the portion of the fiber where the acoustic wave is applied: comparison between the reference signal and the simple FFT (5.15a) and normalized FFT (5.16b). 54
5.16 Signal filtered with a high-pass filter: FFT around the perturbed portion (5.16a) and time-domain visualization (5.16b) with a zoom for $t \in$[1, 1.5] s. 55

Listing of tables

2.1 Some examples of spatial resolution $\Delta/2$ for a given pulse width τ. 12

3.1 Performance of distributed and quasi-distributed sensing techniques [5]. 21

4.1 Comparison between the two EDFA specifications. 27

1

Introduction

The idea of using optical fibers for sensing purposes is almost as old as the idea of using them as transmission mediums [6].
As highlighted in many books and papers, optical fibers have some great advantages that make optical fiber sensors much better and more versatile with respect to electrical and mechanical ones.
Indeed, fiber optic sensors are little intrusive, passive and intrinsically immune to electromagnetic interactions. Moreover, some of their characteristics make them particularly suitable for harsh environments.
What makes optical fibers unique among all the other sensing techniques, however, is the capability of monitoring physical fields, such as temperature and strain, in a distributed way, all along the fiber length.
These kinds of sensors are called *distributed optical fiber sensors (DOFS)* and their main characteristic is that the whole fiber acts as a sensor, differently from point and quasi-distributed sensors (Fig. 1.1).
This characteristic, along with the possibility to embed the optical fiber in structures such as bridges, buildings, power generators, airplanes and other civil works make them one of the best sensing technique for these kinds of structures. Indeed, among the main fields of application of DOFS, we can find civil infrastructures and pipelines monitoring.

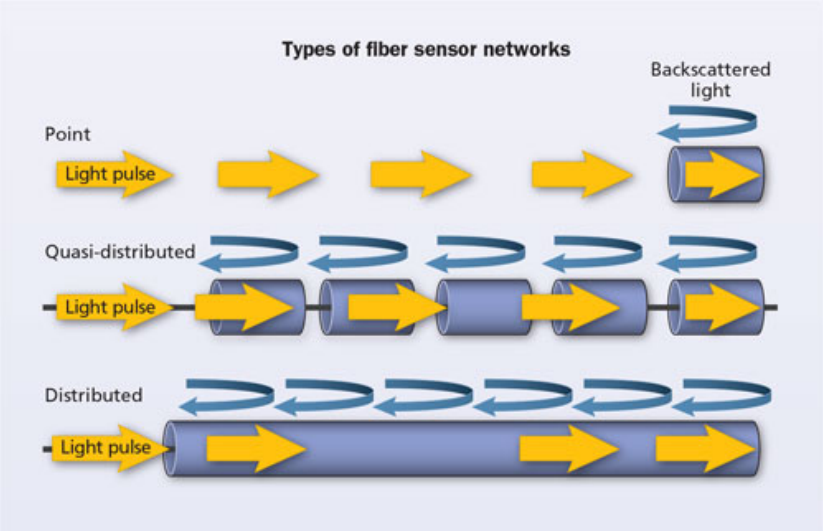

Figure 1.1: Different kinds of fiber optic sensing [1].

These distributed optical fiber sensors exploit the scattering processes that take place inside the fiber itself and probe it with proper interrogation systems; in such a way, they can map the required physical fields.
Inside optical fibers, three different scattering phenomena take place: Rayleigh, Raman and Brillouin, and each of them can be exploited for different sensing purposes. In fact, when probing the fiber with an appropriate signal, it is possible to extract information about the local properties of the fiber by analyzing the back propagating signals.
However, each scattering behaves in a different way and is sensitive to different parameters. For example, since the intensity of Raman scattering is intrinsically dependent on the temperature of the fiber, it is largely exploited to implement distributed temperature sensors (DTS). On the other hand, the frequency of Brillouin scattering is dependent on the density of the fiber, which in turn can vary with both temperature and strain; this property is highly exploited in the design of temperature and strain distributed sensors. Lastly, Rayleigh backscattering can be used to extract information about the fiber, that can in turn be exploited for distributed sensing. Among the techniques that make use of Rayleigh scattering, there is the ϕ-OTDR, a phase-sensitive optical time domain reflectometer that analyzes the back scattered power and is employed as a distributed acoustic sensor (DAS).

The aim of this thesis is the design of such a kind of sensor: a ϕ-OTDR setup has been implemented and its correct working has been tested through the application of different kinds of acoustic waves. The traces have been acquired with an acquisition board and then analyzed with Matlab.

1.1 Guide to Reading

This thesis is structured as follows:

- In **Chapter 2** we focus on the theoretical background that is useful to understand the principles of ϕ-OTDR technique. In particular, we concentrate on the Rayleigh scattering and how it is analyzed through the OTDR. Then we explore the ϕ-OTDR technique and its use as a distributed acoustic sensor.
- In **Chapter 3** we make a general overview of Distributed Optical Fiber Sensors. We illustrate the main domains in which the different scatterings are exploited and the results achieved in terms of spatial range and resolution, by referring to some relevant works about each kind of sensor.
- **Chapter 4** shows how the ϕ-OTDR has been implemented. At the beginning, we give a general description of the components and of the working principle. Then, some of the most important instruments are analyzed more in detail, in particular the acquisition board and its acquisition methods. Moreover, we introduce the key parameters of our OTDR setup and some information about the data analysis.
- **Chapter 5**, finally, concentrates on the acquisition results. We show both simple ϕ-OTDR traces in different conditions, and the result of the application of different acoustic waves on a portion of the fiber.

2

Theoretical background

2.1 Rayleigh scattering

When a signal propagates into an optical fiber, as for all the other waveguides, it is submitted to some form of attenuation.
In the case of dielectric waveguides, as fibers are, we can distinguish between *absorption losses* and *radiation losses*.
Absorption losses refer to the conversion of the electro-magnetic energy into other forms of energy, typically heat. They can be subdivided into two sets: those which characterize the material (i.e., they are intrinsic), and those which are induced by the presence of some impurities in the material. The latter ones are technology dependent, and that is the reason they are almost negligible in modern optical fibers, except for the peak centered at 1400 nm and caused by hydroxyl ions.
Also in the case of radiation losses, we can distinguish between an intrinsic phenomenon, which cannot be avoided, and external contributions.
What we are interested in for optical fiber sensors is the intrinsic part, due to the scattering phenomena. They originate from the density fluctuations that can be observed on a microscopic scale in an amorphous material, such as glass. These fluctuations turn into fluctuations of the refractive index [7]. This phenomenon is called **Rayleigh scattering** and it was modeled since the late 19th century.

This scattering occurs uniformly in the entire volume of the fiber and it is proportional to the amplitude of the local field, so that the attenuation is essentially the same for all guided modes.
The phenomenon strongly decreases with the wavelength, since it is proportional to $\frac{1}{\lambda^4}$, where λ is the signal wavelength.
It might be interesting to know that Lord Rayleigh developed his theory as an explanation for the blue color of the sky.

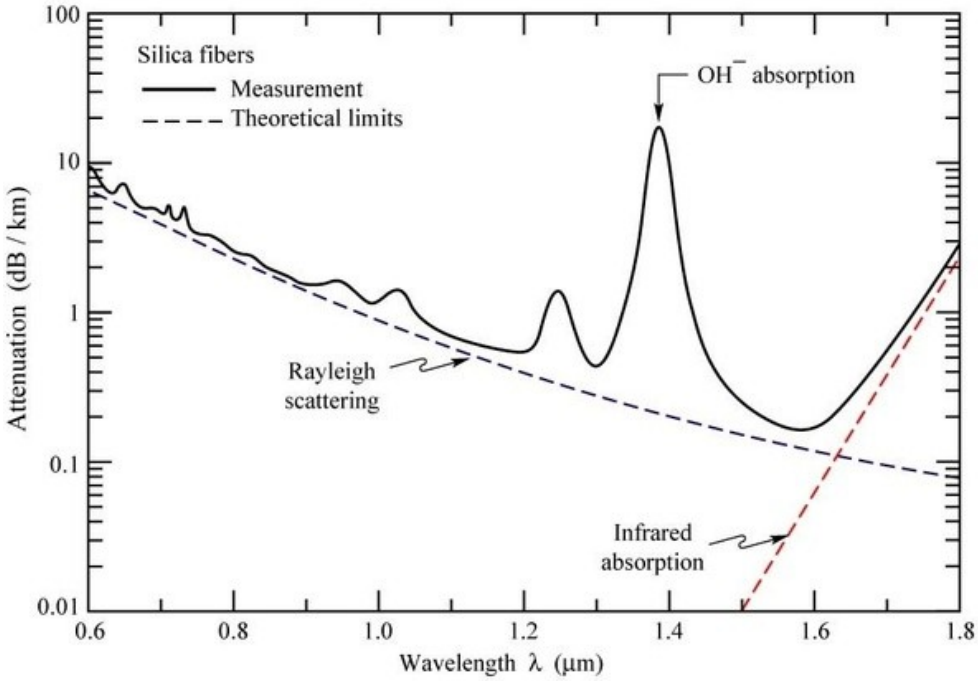

Figure 2.1: Attenuation in optical fibers. The solid line represents the measurement results, while the dotted lines are the theoretical limits due to Rayleigh scattering and molecular vibrations.

When Rayleigh scattering occurs in an optical fiber, the light is scattered in all directions, but part of it is captured by the guiding structure of the fiber itself and is back propagated to the fiber input. Fig. 2.2 reports a schematic diagram of the spontaneous Rayleigh scattering. The parameter $\Delta\varepsilon$ represents the microscopic portion of the fiber with density fluctuations.

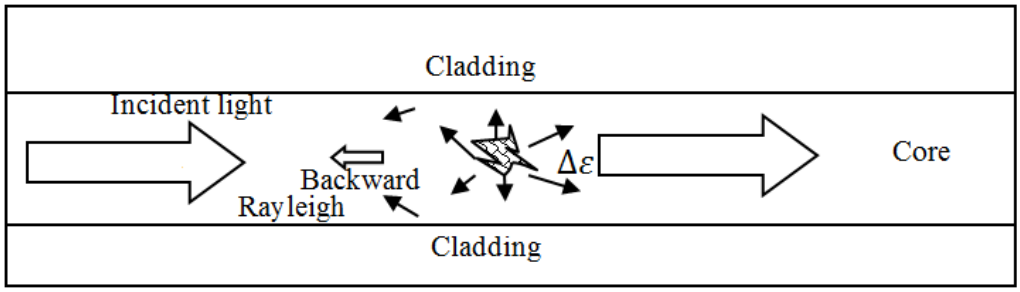

Figure 2.2: Schematic diagram of the spontaneous Rayleigh scattering process [2].

Moreover, during Rayleigh scattering, no energy is transferred to the glass, therefore there is no shift between the frequency of the incident light and the frequency of the scattered light. So, we talk about an *elastic scattering*.
On the other hand, other kinds of scattering are called *inelastic*, i.e. Raman and Brillouin scattering, since they are associated with some changes in frequency. In Fig. 2.3 the typical spontaneous scattering spectra are reported.

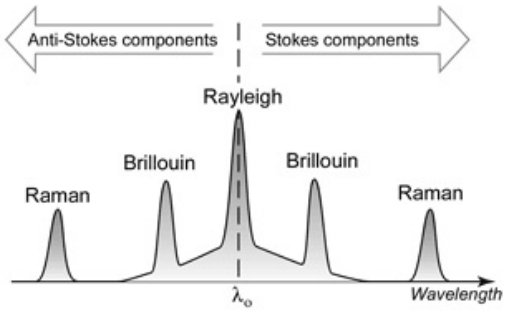

Figure 2.3: Typical spontaneous scattering spectra.

2.2 OTDR

The backscattered light from Rayleigh scattering is exploited by the optical time domain reflectometry (OTDR), which was first proposed in 1976 by Barnoski and Jensen.
Its main purpose is the evaluation of the attenuation in optical fibers, through which the length and the losses of a link can be characterized.

Fig. 2.4 represents the operating principle of an OTDR: from an optical source, typically a laser, the light pulse is sent into the fiber. During its propagation, this pulse is affected by an exponential attenuation, such that the optical power of a given point with longitudinal coordinate z in the fiber is given by:

$$P(z) = P_0 \, e^{-\alpha z} \tag{2.1}$$

where P_0 is the initial power and α the attenuation coefficient.

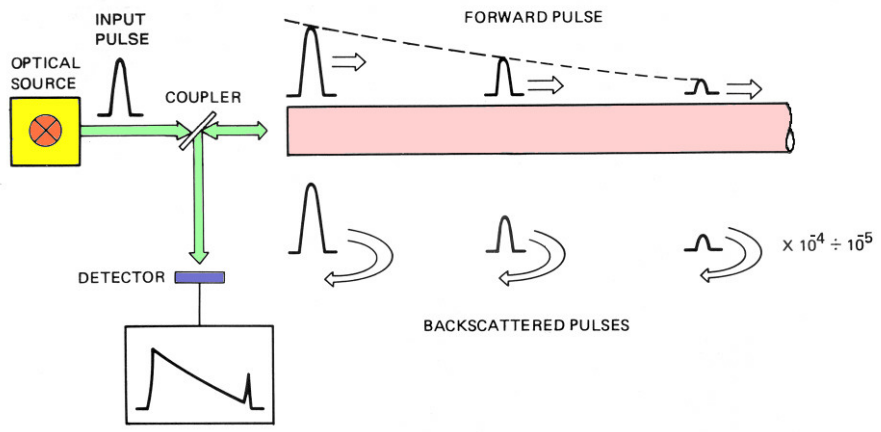

Figure 2.4: Operating principle of an OTDR.

In the same generic point z, Rayleigh scattering generates a counter-propagating pulse, the intensity of which is proportional to $P(z)$ according to a coefficient ρ. In turn, this scattered power undergoes the same attenuation α. In this way, the total power coming back to the beginning of the fiber is $\rho P_0 \, e^{-2\alpha z}$.
Let v_g be the group velocity of the pulse; the roundtrip time t needed by the pulse to get back to the beginning of the fiber is

$$t = \frac{2z}{v_g} \tag{2.2}$$

This means that the backscattered power received at a given time t comes from

a point of the fiber at a distance

$$z = \frac{v_g t}{2} \tag{2.3}$$

We can write the received power as

$$P_r(t) = \rho P_0 \, e^{-2\alpha z} \tag{2.4}$$

where t and z are related by Eq. (2.2).
A coupler sends the backscattered signal to a photodiode, that registers the temporal evolution of the received power.
If the attenuation would be constant, as we have considered it, the trace would be similar to a straight line with negative slope. Otherwise, the trace can have some discontinuities, if the fiber presents some losses due to ruptures, bending, splices, etc. In this case, the trace might be similar to the one in Fig. 2.5.

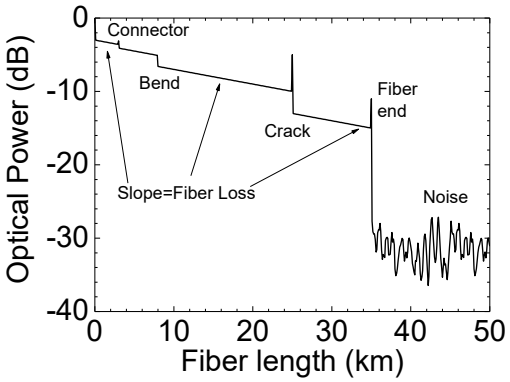

Figure 2.5: Example of an OTDR trace.

There are some **specifications** characterizing the performances of an OTDR. Here we are going to list some of them.

- **Deadzone** We can have deadzones close to the reflections, when the OTDR receiver saturates, due to the reflected optical signal. Whenever a too high signal saturates the receiver, it is then necessary to wait some time for the receiver to recover. We can distinguish between two kinds of deadzone:

event deadzone and attenuation deadzone.
We talk about event deadzone when we measure the distance between the beginning of a reflection and the point which is at -1.5 dB from the reflection peak on the trailing edge of the reflection. After this distance, it is already possible to measure an adjacent event.
The attenuation deadzone instead is measured as the distance between the beginning of a reflection and the position where the receiver has regained a marge of ± 0.5 dB with respect to the backscattering trace. After this distance, the OTDR can work again.

- **Dynamic Range.** It specifies the maximum power loss between the beginning of the backscatter and the noise peaks. If the loss is higher than this range, the far end disappears in the noise. This parameter is highly dependent on the setup. The main influences are the pulse width, the optimization mode and the wavelength. The dynamic range also determines the maximum length of the link that can be analyzed, i.e. the *spatial range*, which is one of the key parameter characterizing the distributed sensors.

- **Spatial Resolution.** This is another key parameter for the distributed sensors. It represents the minimum distance at which two consecutive events can be detected.
The width of the pulse sent into the fiber gives the lower bound to the spatial resolution.

To better understand the principle of the spatial resolution calculations, we can consider a pulse of duration τ, where typically $\tau \in [10^{-8}, 10^{-6}]$ s for the OTDR. The length of the pulse in the fiber will be then:

$$\Delta = \frac{c}{n}\tau \tag{2.5}$$

where $c \approx 3 \cdot 10^8$ m/s is the speed of light in the fiber and $n \simeq 1.5$ the refractive index of the fiber.
With the values of τ considered above, we can get to $\Delta \in [2, 200]$ m.
Since the duration of the pulse is quite high with respect to the pulse used in

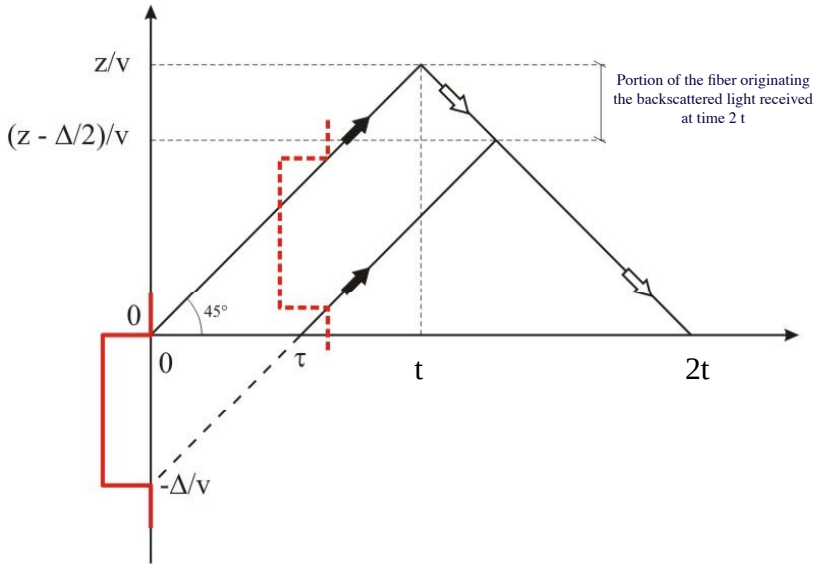

Figure 2.6: Minkowski diagram.

telecommunication systems, the dispersion effects can be neglected.
An useful tool that allows to understand how the spatial resolution is related to the pulse width is the **Minkowski diagram**, which is represented in Fig. 2.6.
We can start the analysis with a rectangular pulse, which has an evolution in the time and space domain given by $\text{rect}\left(t - \frac{z}{v}\right)$. The Minkowski diagram represents its evolution on the plane $\{t, \frac{z}{v}\}$, where v is the group velocity of the pulse. The pulse enters the fiber at time $t = 0$. While time goes on, the signal follows a straight trajectory, meaning constant velocity. This line forms an angle of 45° with respect to the axis. Suppose now to have backscattering in the point $\frac{z}{v}$, corresponding to time t. The backscattered signal will have the same straight trajectory as the propagating light, but on the opposite side, so it will arrive back to beginning of the fiber at a time $2t$. At the same time $2t$, we will receive also the backscattered light from the tail of the pulse, which we can say t', and all the contribution in the middle. So, at instant $2t$ the detector receives the superposition of the backscattering in the time interval $[t, t']$, corresponding to the space interval $\left[\frac{z-\Delta/2}{v}, \frac{z}{v}\right]$, of length $\frac{\Delta}{2}$.
We have proved that the spatial resolution of the instrument is $\Delta/2$: the receiver cannot distinguish between two events that happen at a distance less than or

equal to this length.
Table 2.1 shows some examples of spatial resolution for a given pulse of length τ, according to Eq. (2.5).

τ	10 ns	100 ns	1 μs	10 μs
$\frac{\Delta}{2}$	1 m	10 m	100 m	2 km

Table 2.1: Some examples of spatial resolution $\Delta/2$ for a given pulse width τ.

However, as mentioned above, in the case of DOFS, the spatial resolution should be considered as a lower bound to the resolution. Indeed, the spatial resolution of a DOFS, i.e. the spatial accuracy with which the sensor can map the physical space, depends also on other factors, such as the signal to noise ratio of the measurement.

2.3 Phase-sensitive OTDR

While analyzing the OTDR, we have considered an incoherent light source, i.e. with a small coherence length. As a consequence, we have neglected the **interference terms**, that show the interference between different scatters within the same pulse. In fact, they disappear at the receiver side in case of incoherent light. On the other hand, if we use a **high coherence laser** as a light source, we can measure them; this is the working principle of the phase-sensitive OTDR (ϕ-OTDR).
Its structure is similar to the one of the OTDR, but it uses a high coherence narrow-band laser as a light source.
In order to better understand how it works, we consider the intensity of the backscattered power received by the photodetector. It is the sum of all the fading contributions coming from all the small scattering centers. Each of them can be written as

$$E_m = E_{in} r_m e^{j\phi_m} \tag{2.6}$$

where E_{in} is the incident field, r_m the reflection coefficient of the scattering center m and ϕ_m its phase.

The received intensity from M scattering centers will be then

$$
\begin{aligned}
I_{backscattered} = |E|^2 &= \left| \sum_{m=1}^{M} E_m \right|^2 \\
&= |E_{in}|^2 \left[\sum_{m=1}^{M} r_m^2 + \underbrace{2 \sum_{i=1}^{M-1} \sum_{j=i+1}^{M} r_i r_j \cos(\phi_i - \phi_j)}_{Interference\ terms} \right]
\end{aligned}
\tag{2.7}
$$

As highlighted in Eq. (2.7), the last terms are the results of the interference of several backscattered fields, that interfere in a random way, since the phase of each single contribution is random $\in [0, 2\pi]$.
In particular, $\phi_i - \phi_j$ is the relative phase of the i-th to j-th scattering centers of the backscattered wave [3].
Thanks to these terms, given a point of the $\phi-$OTDR trace, in this point the system is sensitive to the phase of the light at that position. So, if the refractive index changes at a given point, this leads to a variation of the phase, that may be seen as some kind of disturbance.
Fig. 2.7 shows a typical ϕ-OTDR trace, with its "noise-like" characteristic shape.

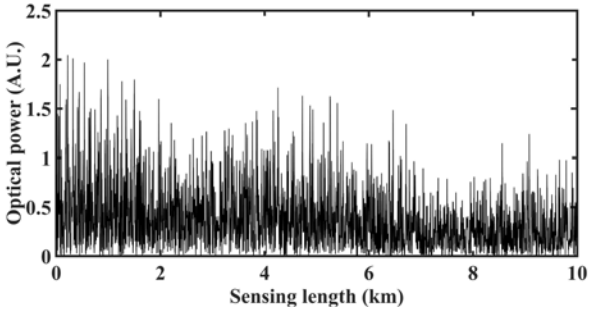

Figure 2.7: Simulated ϕ-OTDR trace [3].

As in the case of the simple OTDR, the spatial resolution of the instrument is half the pulse width: the shortest the pulse, the highest the spatial resolution; however, it is necessary to find a trade-off, because a smaller pulse means also a lower SNR, when the ϕ-OTDR is used for long range measurements.

2.4 ϕ-OTDR as a Distributed Acoustic Sensor

In spite of its characteristic pattern, the ϕ-OTDR trace should remain almost constant in time. In this way, if we perform many different consecutive acquisitions of the same trace, we might have the same shape, if no perturbation has occurred on the fiber.
On the other hand, if an acoustic wave is coupled to a portion of the fiber, it interacts with it and changes the refractive index.
Considering an acoustic wave propagating along the x direction, it can be described as

$$s(x,t) = S_0 \cos(\Omega t - qx) \tag{2.8}$$

where $\Omega = 2\pi f$ is the angular frequency, and $q = \frac{2\pi}{\Lambda}$ is the wave number, with $\Lambda = \frac{v_s}{f}$ and v_s the propagation velocity.
The induced variation of the refractive index of the fiber is proportional to the acoustic wave according to the following equation:

$$\Delta n(x,t) = -\frac{1}{2}\, p\, n_0^3\, s(x,t) \tag{2.9}$$

where p is the photoelastic constant, typically considered ≈ 0.25 in the case of glass.
The refractive index can then be modeled as follows:

$$n(x,t) = n + \Delta n(x.t) = n - \frac{1}{2}\, p\, n_0^3\, S_0 \cos(\Omega t - qx) \tag{2.10}$$

In the case of the ϕ-OTDR, this change happens in that portion of the fiber affected by the vibration. As a result, we can see a local change of the trace around the perturbation zone. An analysis of the consecutive traces in the frequency domain allows to recognize also the exact frequency of the acoustic wave.

In this thesis, a ϕ-OTDR setup is implemented, in order to detect different frequency vibrations at a given point of a fiber coil.

3

Overview on Distributed Optical Fiber Sensors (DOFS)

The nature of optical fibers and their characteristics make them excellent sensors. We could say that the fibers can behave as a sort of nerve system [8]. Indeed, an optical fiber can be used to perform distributed measurements over long distances and in wide ranges. Moreover, it does not need an external electrical power supply, it is not affected by electromagnetic interference and it has a great sensitivity. It is also light weight, corrosion-resistant and has an excellent durability.

A first kind of fiber optic sensors is given by the **quasi-distributed** sensors. They are comprised of many different point sensors distributed within a single fiber. In this way, just some parts of the fiber are sensitive and can perform the measure. The main advantage of this configuration is that just some small segments need to be controlled and their position to be known. Moreover, they are easier and less expensive than other kinds of sensors.
The fiber Bragg grating based sensors are an example of the quasi-distributed. They exploit the relation between the period of variation of the refractive index inside the fiber and the reflected wavelength. Indeed, a different period leads to

a different reflected wavelength according to the relation

$$\lambda_B = 2n_e\Lambda \tag{3.1}$$

λ_B being the wavelength reflected by the gratings, n_e the effective refractive index of the fiber and Λ the grating period.
Many works focus on the use of FBGs as vibration sensors. Among them, [9], in which the authors modulate the light of a tunable laser reflected back from an FBG. This fiber Bragg grating was glued to a PZT vibrator, and expanded or contracted according to the vibrations of the PZT. The mechanical vibrations could be observed directly by measuring the modulation component of the detected signal. In [10] and [11], the same authors involve the use of a second FBG to select a narrow linewidth from a broadband source, to maximize the signal intensity. Other works, as [12] and [13], use FBGs to detect acoustic emissions. They managed to detect signals at transmitter-receiver distances up to 30 cm.

The limits of the quasi-distributed sensors can be overcome thanks to the **distributed fiber sensors**.
In general, one of them can replace many of the previous kind of sensors. Indeed, the distributed sensors only require a single optical fiber capable of sending and receiving the signal from the same fiber. Moreover, the local changes in temperature, stress, vibration and acoustic wave only need one monitor to be displayed. These advantages, along with the light weight, make distributed sensors the most powerful monitoring option, especially for structural monitoring when the distribution charge is critical for a civil or aerospace structure [2].
Distributed sensors can be realized by using both time and frequency domain analysis of the scattered signals.
Sensors can achieve different performances, especially in terms of spatial resolution and range, depending on the considered signals.

3.1 OTDR based sensors

When they are realized in the time domain, we talk about OTDR sensors.
As seen in Chapter 2, one key parameter of the distributed sensors is the *spatial*

resolution, i.e. the spatial accuracy with which an event can be detected. In the case of OTDR sensors, the spatial resolution is related to the width of the input light pulse.
There are three different types of OTDR sensors, based on Raman, Brillouin and Rayleigh scattering.

Raman scattering is an inelastic scattering, associated with some frequency shifts, that originates the Stokes (down-shifted) peak and anti-Stokes (down-shifted) line. Raman scattering is highly dependent on the temperature of the fiber. For this reason, OTDR based on Raman scattering has been employed for temperature sensing during the 1980s [5].
The principle of Raman temperature sensors is based on the ratio between the intensity of anti-Stokes and Stokes components. The simplest method leads to some errors, since the same fiber attenuates Stokes and anti-Stokes reflected lights in different ways. A large number of improvements have been proposed in order to obtain more accurate results. For example, [14] makes a correction based on the dual end method. Furthermore, [15] proposes the double source light methods.
In spite of the large improvements achieved in terms of sensing range and spatial resolution, we still need to choose a trade-off between them. As we can see in Table 3.1, in [16] the authors have achieved a spatial resolution of 1 cm for a sensing range of 1 km, while in [17] they can achieve a 17 m spatial resolution over a 37 km spatial range.
Monitoring of hot spots in high power transformers for the power supply industry and pipeline temperature monitoring are among the applications of distributed temperature sensors.

Brillouin based OTDR (BOTDR) can achieve better performances than Raman one.
As for Raman, Brillouin scattering is an inelastic scattering and it is caused by the collective acoustic oscillations of the glass. Indeed, these vibrations produce a counter-propagating wave, which weakens the forward-moving input pulse. The energy conservation is guaranteed by the frequency shift between the scattering and the original light pulse frequency.
This phenomenon is highly dependent on the fiber density. In turn, density is

related to temperature and strain. This is the reason why Brillouin scattering is employed for both temperature and strain sensing.
Among the first works focusing on Brillouin temperature sensors, we can highlight [18], [19] and [20].
BOTDR is capable of long-distance distributed measures with quite high sensitivity, thus it can be employed for large-scale applications of structural and geotechnical monitoring.
On the other hand, both BOTDR and BOTDA (Brillouin optical time domain analysis) have limited spatial resolution, of about 1 m. In order to overcome this limit, many works investigated different analysis techniques and algorithms. Among them, we need to mention [21] and [22], that improved the resolution to the cm level.

The last kind of OTDR is **Rayleigh scattering based OTDR**, which was first introduced for fault detection in telecommunication cables, since it can monitor fiber attenuation. Later, it has been employed in a large number of different applications, mainly exploiting the effects of the measurand on the loss of the fiber.
There are several types of Rayleigh OTDR systems and each of them can be used for different sensing purposes and techniques. We will now analyze some of them.

- *Conventional OTDR.* The simplest kind of OTDR can be exploited for sensors based on bending effects, that have to be mechanically introduced through an external structure [6]. Among these, the most common solutions are based on micro-bending, induced on the fiber thanks to a periodic structure applied around it.
  This idea was first proposed in 1989 and it consisted of a periodic metallic coating applied on a fiber; thus, it became sensitive to temperature, pressure and hydrogen molecules [23].
  Some years later, more accurate and feasible solutions have been explored, as we can see in [24]. This structure involves a multimodal fiber and a simple OTDR to monitor contact with water. Indeed, when in contact with water, the system induced some micro-bending on the fiber, whose losses could be detected via OTDR.
  Micro- and macro-bending are involved also in crack detention ([25] and

[26]), strain and deformation sensing [27] and others.
Standard OTDRs are also employed for sensors based on evanescent field interaction. In these kind of sensors, the cladding of the fiber is modified or accurately engineered in order to enhance the interaction between the propagating light and the external environment. In general, these sensors make use of multimodal fibers, which have a thinner cladding. Anyway, the measurement range is limited to about 1 km. The main field of application is chemicals detection. One of the first approach was the detection of water and humidity through a polyvinyl acetate cladding [28]. More recently, different claddings have been proposed, sensitive to other chemicals. For example, hydro-carbons [29], hydrogen cyanide, chlorine and hydrogen sulfide. The sensing mechanism can be either a change of cladding absorption, or an increase of cladding refractive index, thus the fiber guidance is compromised.

- *Polarization-OTDR (POTDR).* Since real fibers are not exactly symmetric, polarization is not maintained during the light propagation in the fiber. Asymmetry can be both a consequence of imperfection during the production process and of external perturbations, as bending or twist, pressure, strain and others. So, polarization of light is sensitive to many different external fields, converting the fiber into a sensor.
  The first idea of a polarization-OTDR was presented in 1980. It was aimed at measuring polarization variation along the fiber for sensing purposes [30]. Even though it was one of the first DOFS ever proposed in literature, it has some problems that make it almost unfeasible for practical and commercial sensing purposes. First of all, spatial resolution is constrained by fiber properties and spatial arrangements, and this arises some technical difficulties. Second, the polarization of the backscattered light is not directly related to the local properties of the fiber, because it is also affected by the roundtrip propagation. For this reason, a strong inverse problem has to be solved through an accurate mathematical model.
  As a consequence, most of the attention around P-OTDR is concentrated on the use of this system for the characterization of polarization properties of telecommunication fibers. In particular, polarization mode dispersion

(PMD) has been studied in order to analyze the quality of fiber optic links [31].

- *Phase-sensitive OTDR (ϕ-OTDR).* Phase-sensitive OTDR exploits the phase interference created by multiple scattering points within the probe pulse. Some noticeable works concentrate on the design of a temperature sensor with the ϕ-OTDR technique. However, vibration sensing is the main application of ϕ-OTDR. Indeed, even though its relaxed constraints on spatial resolution, it allows the use of quite long optical pulses, so the SNR of a single measure can be increased and averaging is not required.
  Anyway, some works concentrate on post processing with averaging techniques, as for example moving average technique [32], in order to improve the acquired data.
  Long-distance range of ϕ-OTDR system has been explored in [33] with different setups. One of them uses a two-channel acquisition in order to collect data from two different photodiodes who receive the signal from a polarization splitter. Thus, the final signal can achieve more stability and a higher SNR because the configuration allows to cancel the fluctuations caused by the changes in polarization.
  These kinds of systems can achieve a spatial resolution in the order of meters. Results can be improved thanks to the use of chirped pulses, as highlighted in [34], where the spatial resolution is pushed up to 1.8 cm.

3.2 OFDR based sensors

The opportunity of achieving a millimeter scale resolution has increased the interest in the frequency domain reflectometer. Indeed, the same resolution in the OTDR system would make the sensor very expensive, because of the strong requirements in terms of acquisition cards and pulse generator.
The spatial resolution of the optical frequency domain reflectometry (OFDR) is depending on the frequency range swept by a tunable laser and is given by the formula

$$\Delta z = \frac{c}{2n\Delta F} \tag{3.2}$$

Sensing Technology	Transducer Type	Sensing Range	Spatial Resolution	Main Measurands
Raman OTDR	Distributed	1 km 37 km	1 cm 17 m	Temperature
BOTDR	Distributed	20-50 km	$\simeq$ 1 m	Temperature and Strain
BOTDA	Distributed	150-200 km	2 cm (2 km) 2 m (150 km)	Temperature and Strain
Rayleigh OFDR	Distributed	50-70 m	$\simeq$ 1 mm	Temperature and Strain
FBG	Quasi-distrib.	$\simeq$ 100 channels	2 mm (Bragg length)	Temperature, Strain and Displacement

Table 3.1: Performance of distributed and quasi-distributed sensing techniques [5].

where n is the refractive index of the fiber and ΔF the frequency sweep of the laser.
Differently from ϕ-OTDR systems, OFDRs measure the interference fringes of the Rayleigh scattered light from a tunable laser and a static reference fiber in the frequency domain, instead of directly acquiring the intensity of the backscattered signal.
OFDR-based sensors are excellent for short range monitoring, as we can see in [35], where the sensing range is about 100 m. Anyway, better results can be achieved at the cost of spatial resolution, and of temperature or strain resolution. For example, [36] reported the detection of high loss points with cm spatial resolution over 5 km measurement range with high sensitivity.

In the above sections we have highlighted some of the most representative distributed sensors and the works that explored them, with their strong points and their drawbacks, depending on the adopted technique. Some of these pros and cons, along with some important results that we can find in the literature, are summarized in Table 3.1.

4

Experimental setup

The purpose of this thesis is to design a distributed acoustic sensor with the ϕ-OTDR technique. Before implementing the final working system, some intermediate measurements have been done just on some parts of the setup, to test the functioning of each component.
Fig. 4.1 shows the final result of the DAS setup.
The light source is a **high coherence laser**, which is necessary to develop a ϕ-OTDR, emitting at a central wavelength of 1550 nm. The polarization of the signal emitted by the laser is controlled by a polarization controller, to reduce the intensity fluctuations caused by changes in polarization.
The light is then modulated by an **amplitude modulator**, according to the pulse generated by the **pulse generator**. As we have seen in the previous chapters, the pulse width needs to find a tradeoff between the spatial resolution, the photodiode response and the non-linear effects that may affect the system.
The modulated signal is sent to a 90/10 power splitter. This step is necessary to control the power fluctuations caused by the modulator. Indeed, the 10% branch of the splitter is connected to a power meter. Before starting an acquisition, it is possible to put the pulse generator in a triggered mode. As a consequence, no signal propagates to the receiver, but it is possible to check the noise level through the power meter and to minimize it by changing the pulse amplitude. The other

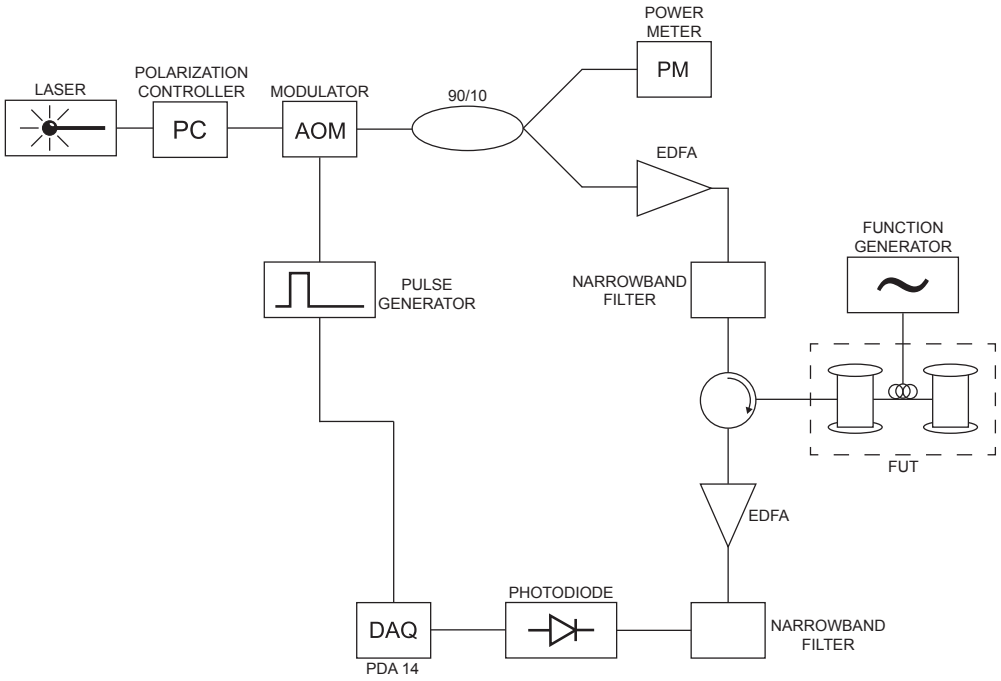

Figure 4.1: Scheme of the distributed acoustic sensor final setup.

branch of the power splitter, instead, is connected to an **Erbium Doped Fiber Amplifier** (EDFA), that amplifies the weak signal coming from the modulator. In turn, the EDFA is connected to a **narrow band filter**, which allows filtering our central wavelength, in order to reduce the effect of the amplified spontaneous emissions generated by the EDFA.
The filtered signal is sent to the first branch of a **circulator**, whose second branch is connected to the coils of **fiber under test** (FUT). They are two coils of single mode fiber, the first has a length of about 1200 m, while the second one is 850 m. These lengths have been previously checked through an OTDR.
A portion of the first coil, of about 20 m, is unrolled and glued to a plastic sheet, then put in contact with a loudspeaker, which allows applying the acoustic vibrations to the given portion of the fiber. In order to generate the acoustic waves, a computer and a function generator have been employed.
The two coils are linked together, while the extremity of the second coil is just closed on a FC/APC connector. Therefore, the backscattered light coming from the fibers is sent to the third branch of the circulator.
Since the backscattered signal is very weak, it is necessary to amplify it with another EDFA, and then to filter with another narrowband filter to reduce the amplified spontaneous emission (ASE).
In the end, the filtered signal is acquired by a **photodetector**, that converts the received optical power into an electric signal. In this way, it is possible to check the amplitude of the ϕ-OTDR trace through an oscilloscope or with a computer and to acquire it.
As we will explain more in detail, the acquisitions have been performed with a Signatec PDA14 acquisition board, an analog to digital converter with 14 bits of quantization.
All the connectors of the setup are FC/APC, i.e., angled connectors, that reduce the back reflections. In a previous version of the setup, the coils had FC/PC connectors, that lead to high Fresnel peaks and some noise disturbing the trace. To reduce these undesired effects, angled connectors have been spliced to the coils, instead of the previous PC connectors.

Now we are going to provide a more detailed description of some of the most interesting components of the setup.

Figure 4.2: Picture of the experimental setup.

4.1 Light Source

The light source (fig. 4.3) is a Distributed Feedback (DFB) fiber laser emitting at a central wavelength of 1550.02 nm at a temperature of 35°C. As already mentioned, it is a narrow band laser, as required by a ϕ-OTDR. Indeed, its line width is < 2 kHz. The maximum emitted power is 19.7 mW, i.e. $\simeq 13$ dBm $\left(P\,[\text{dBm}] = 10\log_{10}\left(\frac{P\,[W]}{1\,mW}\right)\right)$. However, for our purposes, we have used a maximum output power of 11 dBm in order to avoid potential nonlinear effects. The wavelength of this kind of laser can be tuned in two different ways: a thermal wavelength tuning, thanks to a Peltier cell, and a piezoelectric tuning. The first method allows a 400 pm tuning, but is much slower than the second one; the PZT tuning, instead, is faster, but permits a tuning range of 50 pm. This wavelength tuning, however, has not been exploited in our setup, since it was not required for the system implementation.

In the chosen setup, the output of the laser is connected to the modulator, and then amplified. From a theoretical point of view, a pre-amplification configuration

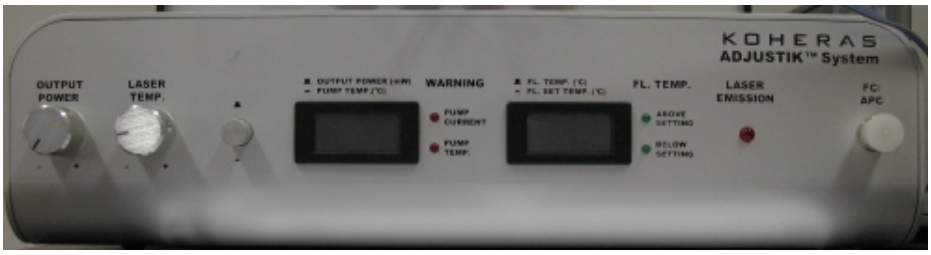

Figure 4.3: Laser Koheras Adjustkit TAdE15PztSpM.

would be preferable, in which amplifier and modulator are inverted, since it can achieve a higher signal-to-noise ratio (SNR). In our specific case, however, the power coming from the laser is quite high, so the direct connection with the amplifier would make it saturate. In such a way, the amplification capabilities would not be entirely exploited. Therefore, the improvements provided by the pre-amplification would be lost. This is the reason the post-amplified condition has been chosen.

4.2 Erbium Doped Fiber Amplifier (EDFA)

In the setup, we make use of two different Erbium-Doped Fiber Amplifiers, one to amplify the output of the modulator, the other for the backscattered light coming from the fiber coils. The two instruments are similar to one another, but not identical, as we can see from the details reported in Table 4.1 and in Figure 4.4.

	EDFA 1 (FA-15)	**EDFA 2 (FA-18)**
Saturated output power	15 dBm	18 dBm
Small signal noise gain	>30 dB	>35 dB
Optical noise figure	<4.2 dB	<5 dB
Input power range	-30 to +10 dBm	-30 to +10 dBm
Wavelength range	1528-1565 nm	1528-1565 nm

Table 4.1: Comparison between the two EDFA specifications.

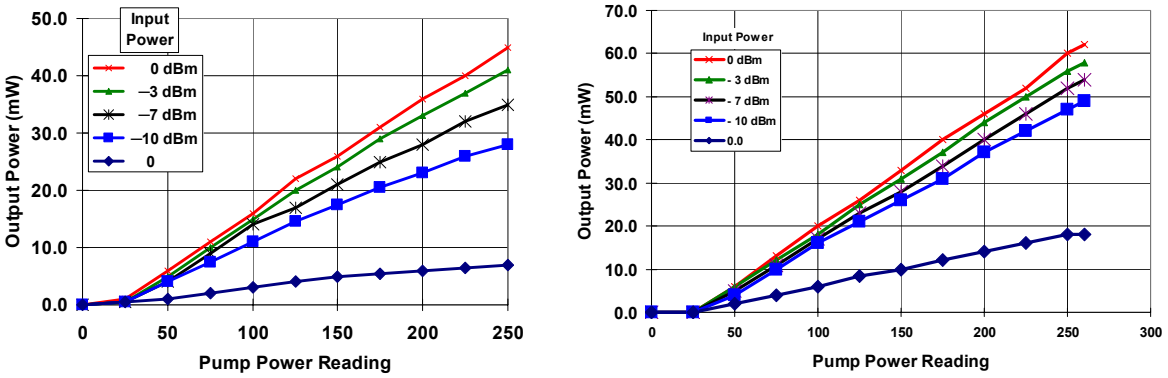

FA-15 FA-18

Figure 4.4: Output power comparison between FA-15 and FA-18.

EDFAs have their maximum gain between 1530 and 1560 nm (fig. 4.5). The actual value of the gain is instead dependent on the pump power. Erbium-doped

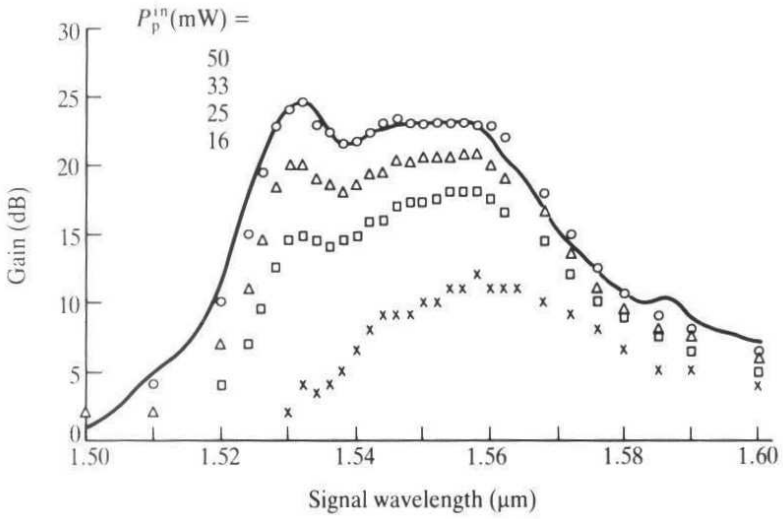

Figure 4.5: EDFA gain. The solid line shows the theoretical limits, while the different markers represent different pump powers.

fiber amplifiers are affected by the phenomenon called amplified spontaneous emission (ASE): some photons are spontaneously generated inside the doped fiber and amplified together with the actual signal. In this way, they create a sort of background noise disturbing the useful signal. The spectrum of the spontaneous emis-

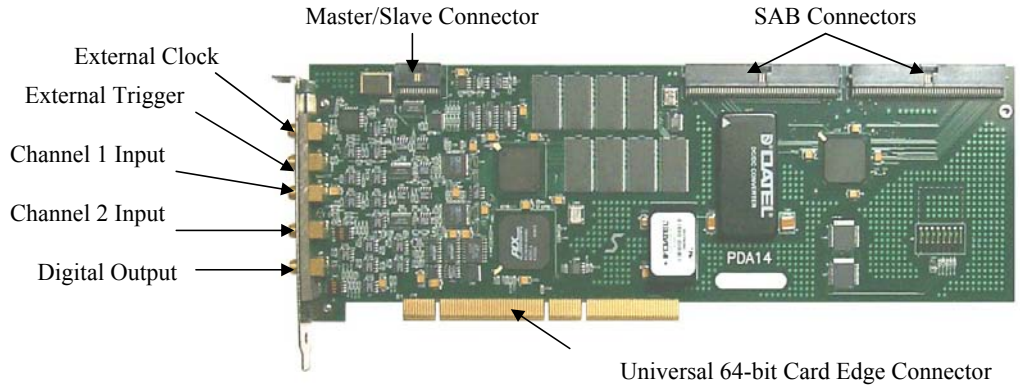

Figure 4.6: PDA14 board [4].

sion follows the gain bandwidth, and it is not negligible at 1550 nm. The power of the ASE measured over an arbitrary bandwidth $\Delta\nu$ with central wavelength ν_s is

$$P_{\text{ASE}}(z) = 2\eta(z)h\nu_s\Delta\nu \tag{4.1}$$

where $\eta(z)$ is the average number of photons per mode of the ASE, and is independent of the input signal, and h is the Planck constant. Even though the ASE cannot be canceled at our central working wavelength, it is possible to reduce it by filtering the signal with a narrowband filter. For this reason, we have introduced the two filters in our setup.
An important EDFA parameter related to the ASE is the Noise Figure (NF), which is the ratio between the input and output OSNR (optical SNR); it measures the impact of the ASE on the quality of the signal:

$$\text{NF} = \frac{\text{OSNR}_{in}}{\text{OSNR}_{out}} \tag{4.2}$$

4.3 Acquisition board

The acquisitions of the data have been performed with the Signatec PDA14 acquisition board, shown in Fig. 4.6. It is a PCI board, with two analog signal channels, each with 256 megabytes of on-board RAM and a maximum digitiza-

tion rate of 100 mega-samples per second. It also implements two high-speed buses: the PCI with a speed of 266 megabytes/s, and an internal Signatec Auxiliary Bus at 500 megabytes/s. The on-board RAM can be used either as the target for the acquired data or as a large FIFO for real-time data acquisitions.
The PDA14 has five external SMA connections: two input channels, a clock input, a trigger input and a user-selectable digital output signal.
Fig. 4.7 shows a schematic version of the PDA14 functionalities.
The board employs 2 14-bit Analog-to-Digital Converters, so each acquired data sample is 14 bits in length. However, to make the manipulation easier, each sample is aligned to 16 bits, the upper two bits being clear. Moreover, each word of the PDA14 RAM contains two samples, the first one in the lower 16 bits, the next one in the upper 16 bits.

4.3.1 Input parameters

There are different modes to perform the acquisitions, and we will analyze them more in detail. However, before starting an acquisition session, whatever is the acquisition method, it is necessary to set some parameters:

- **Number of channels.** We can choose if to acquire through a single channel, either Channel 1 or Channel 2, or with both of them. The maximum number of samples that can be acquired within a single session depends on the number of active channels.
  For this thesis, only one channel is active, since we use a single photodiode to detect the signal.

- **Trigger source.** The trigger source can be external, connected to the corresponding input port, or internal, using directly one of the two channels. We have decided to use the external trigger. Indeed, the trigger signal is sent directly from the pulse generator: whenever a new pulse is generated, a leading edge of the trigger can be detected by the board, which can in this way start a new acquisition of the selected number of samples.

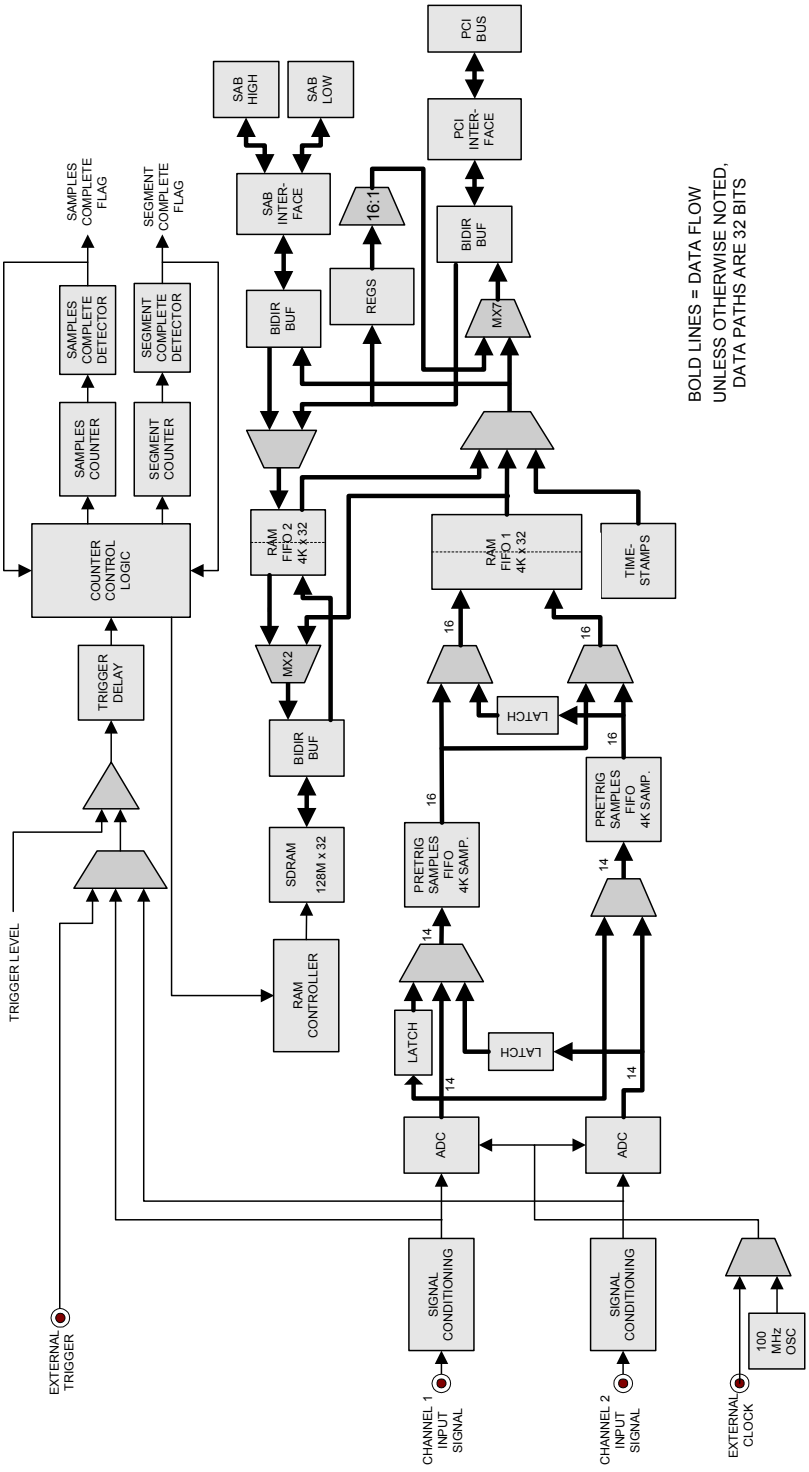

Figure 4.7: Scheme of PDA14 functionality

- **Voltage Range.** This is the maximum range on which the quantization of a sample is performed. It is selected according to the maximum input voltage to acquire and to the precision needed for the samples. Indeed, this parameter affects the conversion into Volt of the acquired data. If we call a sample data s, the conversion to obtain data in the range $\left[-\frac{\Delta V}{2}, \frac{\Delta V}{2}\right]$ V is made according to the following formula:

$$s \text{ [V]} = \frac{s}{2^{14} - 1} \cdot \Delta V - \frac{\Delta V}{2} \tag{4.3}$$

  where ΔV is the selected voltage range. Possible values for ΔV are: 3 V - 1.6 V - 1 V - 600 mV - 333 mV - 200 mV.
  Since the backscattered signal we send to the photodiode is weak, the best choice for our setup is $\Delta V = 200$ mV.

- **Clock.** The board clock can be either internal or external. The internal clock is set to 100 MHz and can be reduced by discarding the undesired samples through the function *clock divider*, which divides the 100 MHz clock by 2^i, where $i \in$[0, 10], such that the minimum value for the clock is 97.656 kHz.
  We have kept the 100 MHz internal clock, to maximize the number of points with which we can characterize the fiber.

4.3.2 Acquisition modes

As previously stated, different acquisition modes are available with the PDA14. We are now going to list them.

- **PCI Acquisition Mode.** With this functionality, data is acquired directly to the PCI bus, then transferred to the system using Direct Memory Access (DMA) transfers. In this mode of operation, the on-board memory is bypassed, and data is passed to the PCI via a 16 kB FIFO.

- **PCI Buffered Acquisition Mode.** This kind of acquisition is similar to the previous one, but in this operating mode the on-board RAM is used

as a giant FIFO to prevent data to be lost, due to periodic hold-off of the PCI data flow due to other system traffic. However, when the data traffic is considerable, the FIFO could overflow.

- **RAM Acquisition Mode.** It is the principal data acquisition method. In this operating mode, the sampling starts at the next detected trigger event. Data is stored on the RAM, and the acquisition continues until the required number of samples has been reached.
  This method is implemented in the `acquireAndTransferP14` function of the PDA14 library: data is acquired to the on-board RAM and then sent to the memory of the computer via a DMA transfer. This mode allows the user to select a maximum number of samples for a single acquisition equal to 2.095 Mega. When the clock is set to its maximum rate (100 Msamples/s), the maximum acquisition time is limited to 21 ms.

To perform continuous acquisitions of the ϕ-OTDR traces, aimed at detecting the acoustic perturbations on the fiber, we have written a new PDA14 function, based on `acquireAndTransferP14`.
This new function is called `repeatedAcquireAndFlush`, and performs nr repeated acquisitions, each of them of ns samples. After every single acquisition, the program writes the recorded data on a binary file called *fileName*. Consecutive traces are written on the same file, just appended at the end of the data of the previous acquisition.
The input parameters required by the functions are the repetition number nr, the time duration of each acquisition t and the *fileName*.
The number of samples needed to reach the required time length is computed as follows:

$$ns = \left\lceil \frac{t}{2^{\text{clockDivider}}/100} \right\rceil_{2048} \tag{4.4}$$

since it has to be the closest multiple of 2048 to the required number.
We have performed some tests to verify the **acquisition rate** at which it is possible to acquire consecutive traces. A first result showed a rate of about 2 kHz, corresponding to a time interval of 500 μs between consecutive traces. The first tests on the setup have been performed at such a rate. Later, some hardware problems may have occurred, since the acquisition rate has decreased to about

1 kHz. Therefore, since then, data is acquired with 1 ms time distance between consecutive traces, thus reducing the maximum detectable acoustic frequency (Sec. 4.4).

4.4 Setup parameters

Different parameters affect the performances of a ϕ-OTDR setup and are related to its spatial resolution, maximum acoustic wave, etc.
Before listing and analyzing them, we need to focus on a preliminary result, conditioning some of the key parameters, and fixed by the fiber under test (FUT).
As already stated in the general description of the setup, we have used two different fiber coils connected through an APC connector. Calling L_1 and L_2 the single lengths of each coil, the total length L of the FUT is

$$L = L_1 + L_2 = 2050\, m \tag{4.5}$$

The **roundtrip time** needed by the propagating light to reach the extremity of the second coil and by the backscattered light to arrive to the photodiode is then

$$t = \frac{2\, L\, n}{c} = 20\, \mu s \tag{4.6}$$

where c is the speed of light in vacuum and n the refractive index of the fiber ($n \simeq 1.5$).
Actually, the calculations in (4.5) should take into account also the length of the patch cords linking the various parts of the setup. However, they can be neglected, as we have done, since their total length is estimated to be about 20 m, and therefore much smaller than the coil length.

Starting from the computed roundtrip time, we are now going to list and calculate the key parameters of the setup.

- **Pulse width and spatial resolution.** As already seen, the pulse which probes the FUT is a square pulse of width τ and repetition period T_p (Fig. 4.8). After having performed some different tests, the pulse width has

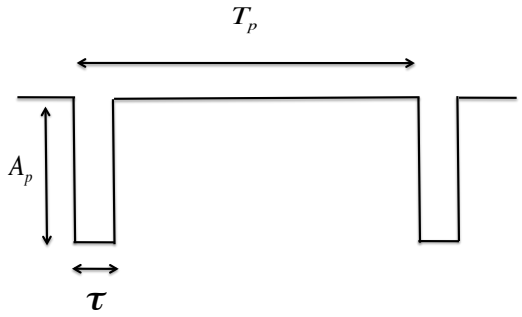

Figure 4.8: Representation of the pulse period T_p and pulse width τ.

been set to τ=150 ns, as a trade off between the spatial resolution and the signal-to-noise ratio. Indeed, a smaller pulse would have required the use of a higher laser power to achieve a useful SNR, thus introducing some non-linear effects. On the other hand, a larger pulse width would have negatively affected the spatial resolution. According to Eq. (2.5), the length of the pulse in the fiber is Δ=30 m, thus the spatial resolution is $\frac{\Delta}{2} = 15$ m.
Along with the spatial resolution, we can consider another spatial parameter that we can call **board resolution**. It gives the number of points per meter of fiber according to the board acquisition rate. Since the clock frequency f_{clock} is set to 100 MHz, in a roundtrip time the PDA14 acquires the following number of samples:

$$n_s = t \cdot f_{\text{clock}} = 2000 \text{ samples} \tag{4.7}$$

As a consequence, we have 2000 points sampling 2000 m of FUT: our board resolution is 1 point/m.

- **Pulse repetition period.** Theoretically, this parameter should depend on the roundtrip time, in fact $T_p > t$ to avoid the superposition of two different pulse while measuring the backscattered signal. However, we have to take into account also the acquisition time, i.e. the time needed by the `repeatedAcquireAndFlush` function to record and save the data of every single trace. As stated in the previous section, this time has changed significantly during the test days. In the last part of the tests, the time needed to record and save a single acquisition was set at about 1 ms.

In this way, for the pulse period we have

$$T_p \geq \max\{t, \text{ acquisition time}\} \quad \Rightarrow \quad T_p \geq 1 \text{ ms} \tag{4.8}$$

The final choice is $T_p = 1$ ms.

- **Acoustic frequency.** The pulse period is related to the sampling frequency: since the board acquires a single trace at each triggering event, and a triggering event occurs at the beginning of each new pulse, the frequency at which traces are sampled is $f_s = \frac{1}{T_p} = 1$ kHz.
  When the vibration is applied to the portion of the fiber, every trace corresponds to an acoustic quantum; so, we can say that we are sampling the acoustic wave with a frequency f_s. According to the sampling theorem, the maximum acoustic frequency that we can detect is

$$f_a = \frac{1}{2} f_s = 500 \text{ Hz} \tag{4.9}$$

- **Pulse amplitude.** The pulse amplitude is given by the difference between the high and the low level selected on the pulse generator:

$$A_p = \text{high level} - \text{low level} \tag{4.10}$$

  The light modulation is affected by these electrical levels: the high level corresponds to the bias point, while the low level regulates the amplitude. To improve the SNR, it is necessary to keep the signal as close as possible to the zero level when the modulator is closed. This can be done by changing the bias point, i.e., by regulating the high electrical level of the pulse.
  The noise level is highly dependent on the bias point, for this reason the power meter has been introduced.

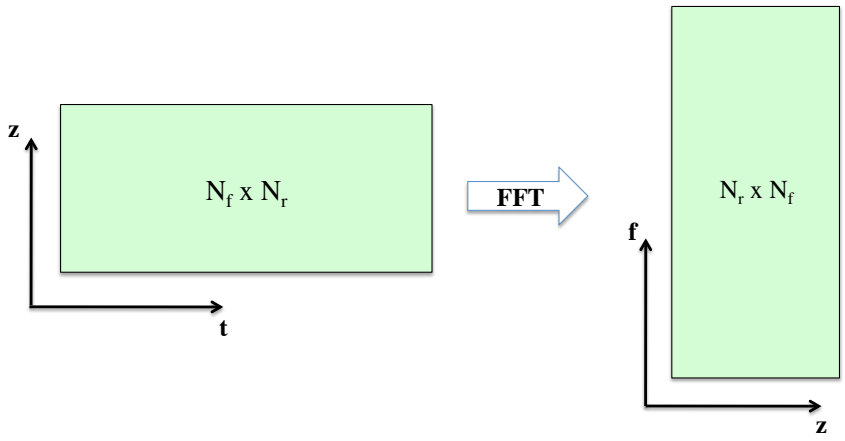

Figure 4.9: Scheme of a data matrix and its FFT.

4.5 Data Analysis

In each acquisition session, we acquire N_r traces, each of them N_s sample long. Typically, we set N_s such that the acquisition time is $T_A > t$, a bit longer than the roundtrip time. In particular, we usually choose $T_A = 25\,\mu s$; in such a way, we have $N_s = 2500$ samples, since the clock is set to 100 Msamples/s.
The data is saved on a binary file, in which different traces are saved consecutively. To better work on the traces, the long stream of binary data is reshaped into a $N_s \times N_r$ matrix. This matrix can be read as a time-space plane: on the x axis (a single row), we have the time, and each cell is spaced of 1 ms; the y axis (a single column), on the other hand, shows the fiber points along the z direction. Later, the exceeding parts along the z directions are removed and the matrix is reduced to $N_f \times N_r$, where N_f is the number of samples corresponding to the length of the coils, i.e., $N_f = 2050$.

To perform analysis in the frequency domain, we use the Discrete Fourier Transform (DFT). Given the sequence $\{x_k\}$ of N elements in the time domain, the DFT is the complex sequence $\{X_k\}$ in the frequency domain, where the k-th element

is computed as follows:

$$\mathcal{F}[x_k] = X_k = \sum_{n=0}^{N} x_n e^{-j\frac{2\pi kn}{N}} \tag{4.11}$$

In our case, the FFT (Fast Fourier Transform) Matlab algorithm has been used to compute the DFT. We apply it to the data matrix, along the time direction t. Thus, we can read the spectrum of each fixed point along the z direction. The new matrix we obtain from the Fourier transform has dimension $N_r \times N_f$, according to the working mode of the Matlab FFT function, which performs the transform on the columns of a matrix. The time direction becomes the frequency direction f. The frequencies must be rescaled, to obtain $f \in [0, f_s]$, where f_s is the sampling frequency. The FFT values are symmetric with respect to $f_s/2$, the useful part of the matrix is then limited to $f_s/2$ along the frequency direction.

5 Results

5.1 Preliminary analysis

Before proceeding with the analysis of the ϕ-OTDR traces, we have performed some preliminary measurements to discover how the background noise affects the setup. The acquisitions have been made in three different conditions:

1. Only the photodiode is connected to the acquisition board. This is the simplest configuration, no working instruments are affecting the measurement, and there are not any signals sent to the PDA14. What is recorded, is just the board and photodiode noise.

2. The setup is completely connected and working, but the laser is turned off. In this way, no useful signals are acquired, only the noise and the ASE coming from the different components.

3. The laser is on and all the instruments are linked to one another, except for the fiber under test, which is isolated from the setup, since we have disconnected it from the circulator. This configuration does not produce any backscattered signal and cancels the noise coming from the fiber coil.

For every different configuration, we have acquired five thousand traces, each of them of 2050 samples, and then averaged along the "z" direction, since it is not

necessary to consider a spatial direction in this noise analysis. Hence, we obtain a vector of 5000 samples, on which we perform the FFT to discover the spectral distribution of the noise.
Figure 5.1 shows the magnitude of the Fourier transform for the three considered conditions. In all of the cases, a peak in $f = 0$ is reported, corresponding to the continuous component. However, as we can see from Fig. 5.1a, the noise level when only the photodiode is connected is almost always below -25 dB, excluding the continuous component. Only a small peak close to -20 dB is highlighted at about 100 Hz. These components, by the way, should not have a great impact on the ϕ-OTDR results. A similar condition is shown in Fig. 5.1b, when the laser is turned off. From this condition, we can say that the ASE of the two EDFAs does not affect significantly the setup.
On the other hand, when the laser is on, but the coils are not connected, we get the results in Fig. 5.1c, where we can see that the absolute value of the FFT has increased of 10 dB in average, so the noise level is considerably higher than in the previous cases.

5.2 ϕ-OTDR traces

As a first test, we have acquired some simple ϕ-OTDR traces with fixed laser output power, P_{out}=12 dBm, and changed the pulse width. Figure 5.2 shows the results in three different cases: T_p=50 ns, T_p=100 ns and T_p=200 ns. As we could expect, a larger pulse width increases the backscatter intensity, hence the SNR. On the other hand, as we have seen in the previous sections, a smaller pulse allows achieving a higher spatial resolution. For this reason, we have chosen a trade-off between the SNR and the spatial resolution, by setting, for the next acquisitions, a pulse width T_p=150 ns.
The graph of Fig. 5.2 highlights also two events characterizing the traces:

1. Starting from the position z=1200 m, we can notice a considerable drop in the backscattered signal intensity. This power decrease is caused by the change in fiber coil. Indeed, the position corresponds to the connection between the first and the second fiber coil.

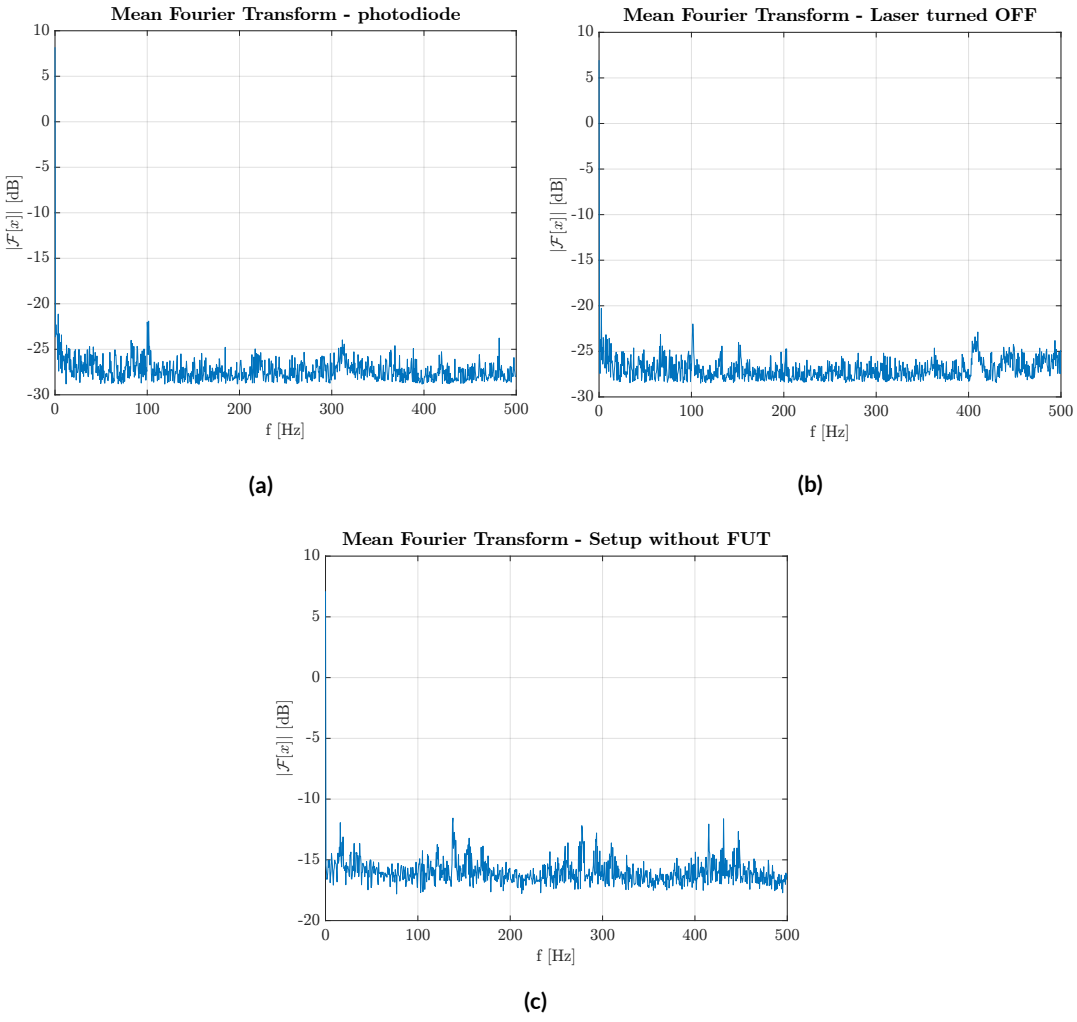

Figure 5.1: Frequency analysis in three different conditions: only the photodiode is connected to the PDA14 (5.1a), the setup is completely connected but the laser is turned off (5.1b) and the FUT is not connected (5.1c).

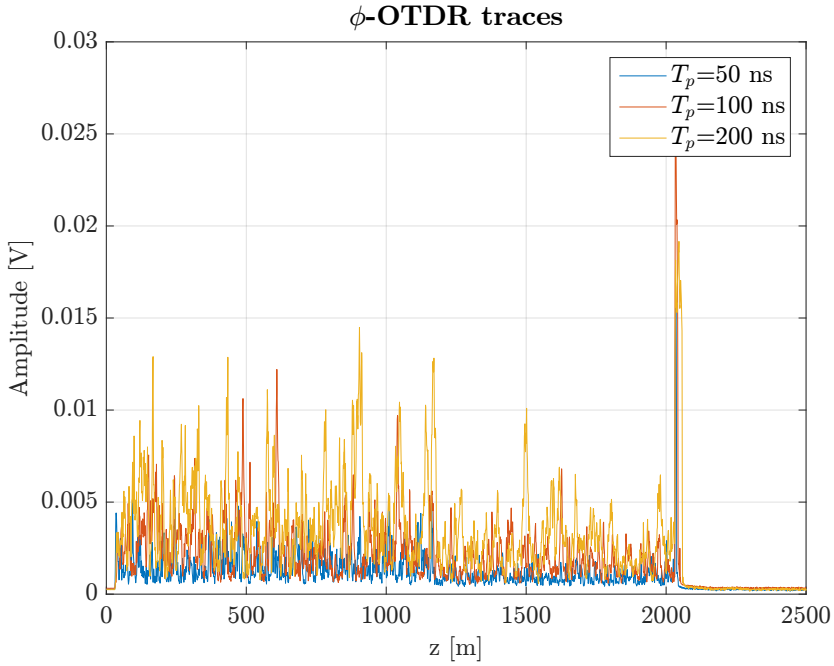

Figure 5.2: ϕ-OTDR traces with different pulse widths.

2. At the end of the fiber, in position $z \simeq 2050$ m, there is the high Fresnel peak caused by the reflections of the last connector.

From a trace, we can also extract information about the fiber attenuation. To this purpose, we consider only the part of the trace corresponding to the first coil. Indeed, the two coils are different and, as stated before, there is a drop in the backscattered power starting from the connection position.
Thus, we have performed a polynomial Least Square Approximation (LSA) on the positions $z \in$[30,1180] m, with a polynomial function of the first degree, i.e. $p(x) = mx + q$. The slope of the curve, m, is the double of the fiber attenuation, $m = 2\alpha$. We have applied the LSA to the ϕ-OTDR trace with a pulse width $T_p = 150$ ns and obtained $\alpha = 0.34$ dB/km. We can consider it close to the theoretical value, $\alpha = 0.29$ dB/km. The result is shown in Fig. 5.3.

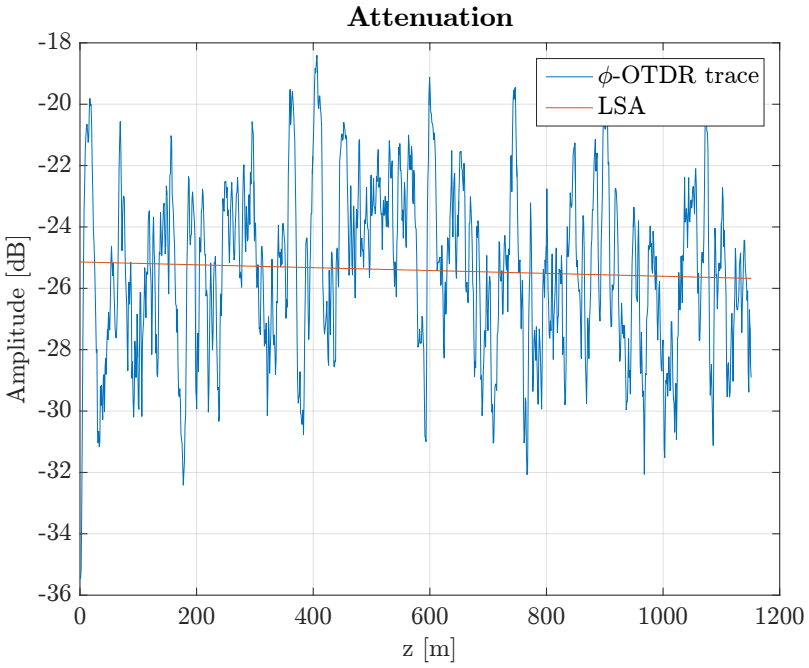

Figure 5.3: LSA approximation of the trace to calculate the attenuation α.

5.3 Acoustic Sensing

To test the setup performances as a DAS, we have applied different acoustic waves to the unrolled portion of the fiber. The waves were sinusoidal functions generated by a function generator and sent to the input of a loudspeaker, that amplified the wave and coupled the vibration to the fiber. The wave generated by the wave generator is

$$v(t) = \frac{V_{PP}}{2} \sin(2\pi f_a t) \tag{5.1}$$

For the amplitude, in general, we have set $V_{PP} = 800$ mV, corresponding to the peak-to-peak value. To test the performances and frequency resolution of the ϕ-ODTR, the frequency f_a has been changed from $f_a = 50$ Hz to $f_a = 500$ Hz, the maximum detectable acoustic frequency for our setup, with a step of 25 Hz. In all the cases, it has been possible to detect the correct frequency.
Different signal analysis have been performed to see the results.

As a first test, we have computed a simple FFT on the data matrix, as described

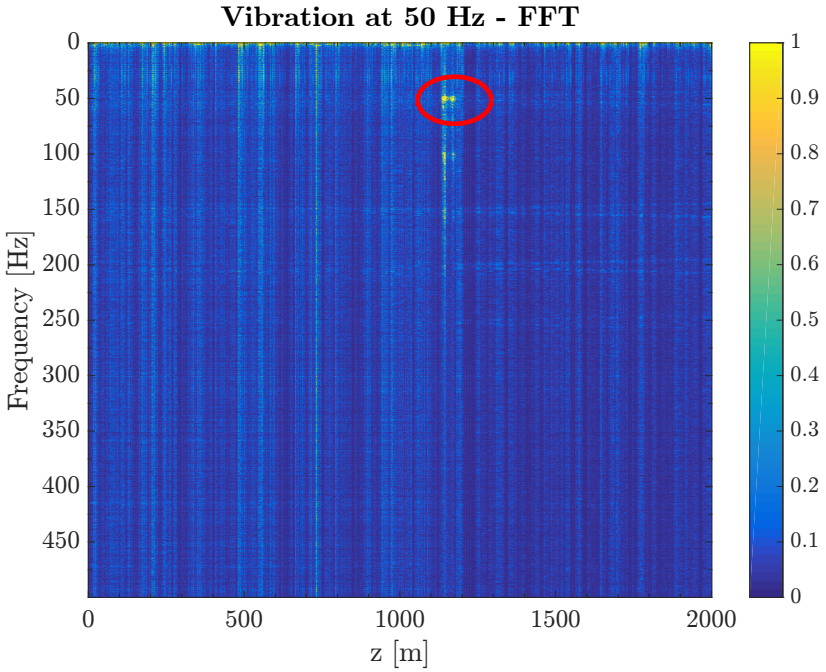

Figure 5.4: Spectrogram of the ϕ-OTDR when a perturbation with $f_a = 50$ Hz is applied.

in Section 4.5, and observed its spectrogram.

We can see an example of this spectrogram for $f_a = 50$ Hz in Fig. 5.4. The x axis represents the position along the fiber, according to a reference parallel to the fiber axis; we have considered the first 2000 meters of fiber. The y axis, instead, shows the frequencies. The colors of the spectrogram represent the intensity of the FFT absolute value for the given position and frequency, according to the colormap on the right. As we can see, there is an intensity peak for $f \in [48, 53]$ Hz and z around the perturbed portion of the fiber, $z \in [1140,1180]$ m. This peak corresponds to the Fourier transform of the sinusoidal wave: we can say that the vibration has been correctly detected. A zoom on this position is shown in the 3-D surface plot in Fig. 5.5.

If we get back to the analysis of Fig. 5.4, we can notice that along the same position we can see two other peaks, with lower intensity, the first at about $f = 100$ Hz and the second around $f = 150$ Hz. They correspond to the higher harmonics, and are caused by overmodulation of the signal.

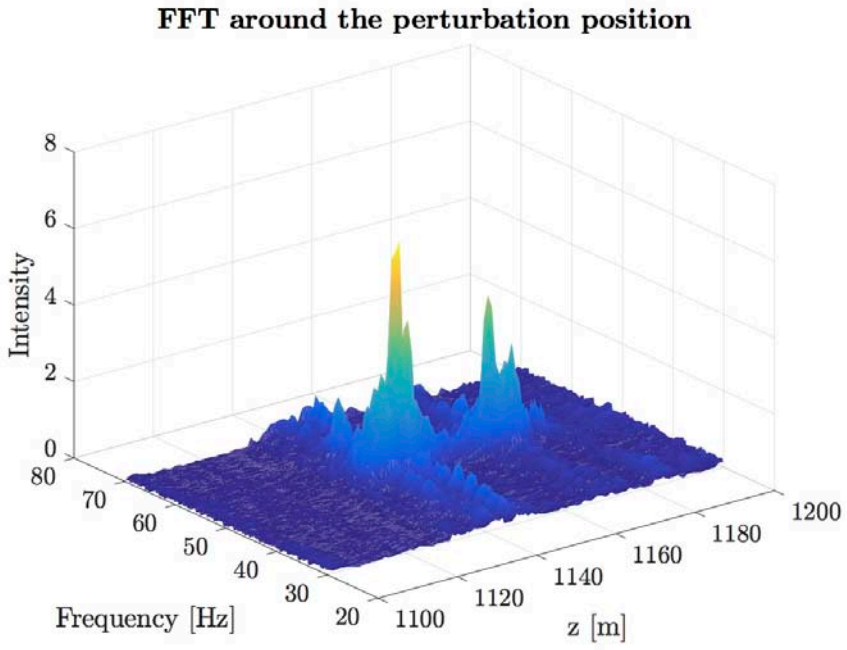

Figure 5.5: 3-D zoom on the FFT around the point of application of the perturbation.

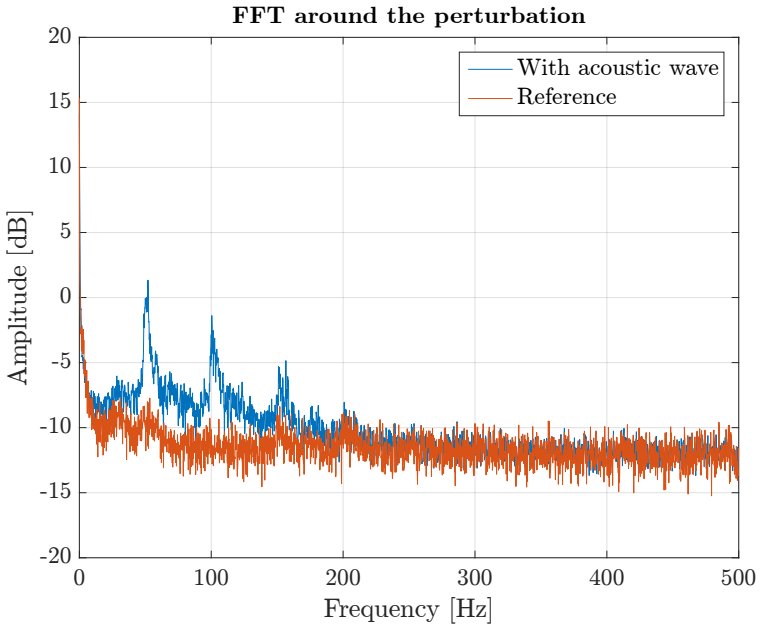

Figure 5.6: Mean FFT around the perturbed portion of the fiber: comparison between reference and acoustic wave.

We can further inspect the Fourier transform by averaging the signal around the area of application of the acoustic wave. In particular, we have averaged the portion of the fiber with $z \in [1130, 1180]$ m. Then, we have compared it with the mean Fourier transform in the same position, but in a reference case, acquired when the pulse generator was turned off. As Fig. 5.6 shows, there is a visible peak around $f_a = 50$ Hz, and also its higher harmonics, with $f = 100$ Hz and $f = 150$ Hz can be detected. The three peaks do not appear in the reference spectrum.

After this first analysis of the FFT, we have employed other techniques to increase the SNR of the acquired traces and to emphasize the vibration frequency.

Since the amplitude of the backscattered light is not constant along the fiber, it is useful to normalize the values of the Fourier transform with respect to its average for each z position. Thus, the mean value of the FFT magnitude has been computed along the z direction, then all the amplitudes have been divided

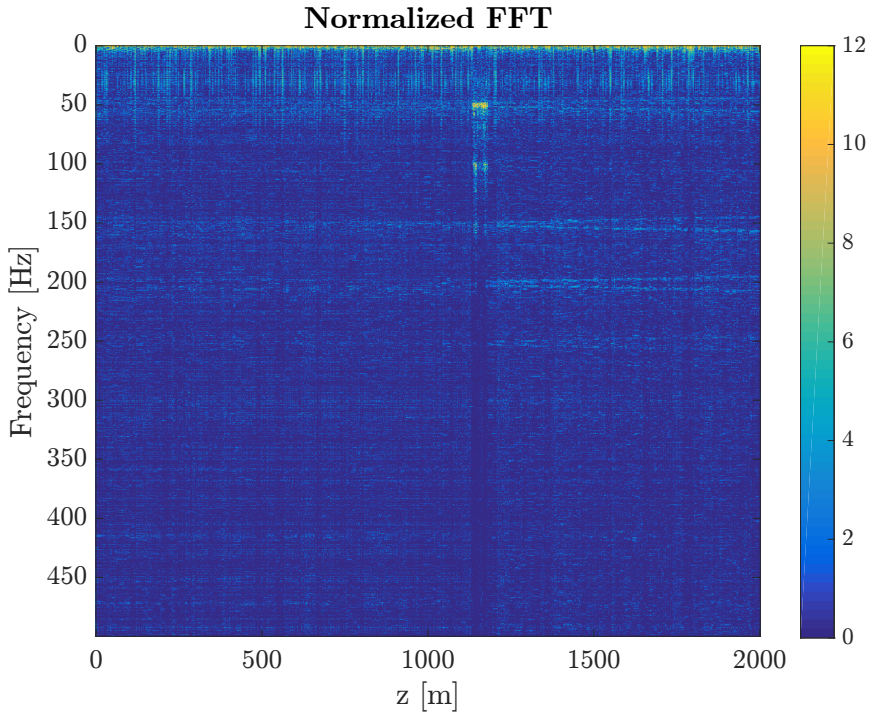

Figure 5.7: Normalized FFT when a perturbation of f_a=50 Hz is applied.

by the corresponding average. Fig. 5.4 shows the spectrogram; amplitude is in dB unit. The normalization has amplified the continuous component, but allowed to reduce the noise in the spatial range $z \in$[1130, 1180] m, corresponding to the portion of the fiber affected by the perturbation. Moreover, the amplitude of the higher harmonics have been reduced with respect to the component at $f = 50$ Hz. Also in this case, we have inspected the FFT around the position of application of the perturbation (Fig. 5.8). As we can see, the difference between the peak in $f = 50$ Hz and the first higher harmonic has increased to 5 dB, while the second higher harmonic is considerably lower.

In both cases, the simple FFT and the FFT normalized with respect the mean value, we can see some noise and the continuous component of the spectrum. To reduce the continuous component, two methods have been proposed.

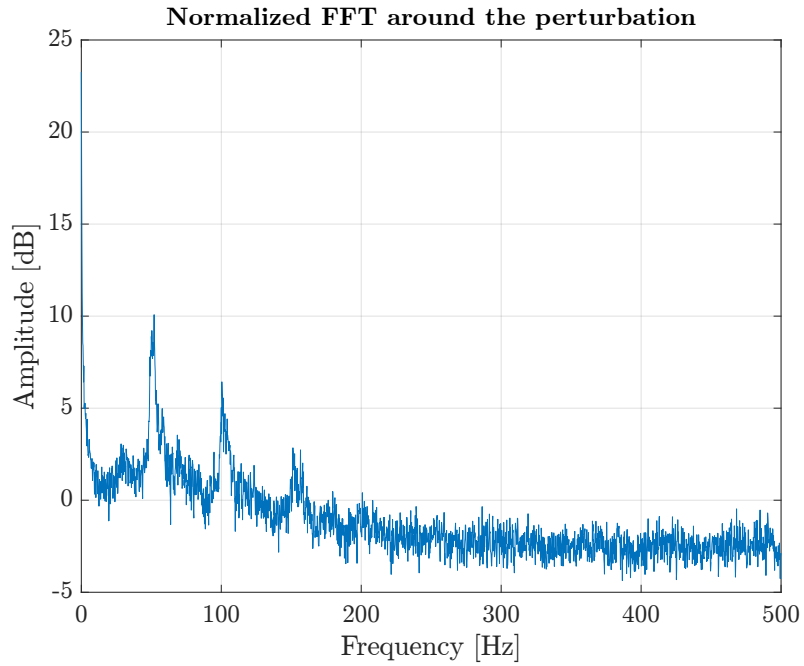

Figure 5.8: Normalized FFT around the acoustic wave position.

The first one is simple filtering of the trace with a high pass filter, with cut frequency $f_c = 5$ Hz, which cuts off the continuous component. The result is shown in Fig. 5.9.
The spectrum we have obtained is the Fourier transform of a sinusoidal signal, which can be seen by simply analyzing the averaged signal in the time domain. Fig. 5.10 shows the evolution of the backscattering in the region $z \in [1130, 1180]$ m during a period of 5 seconds. The same graph also represents a zoom for $t \in [1, 1.5]$ s, to better highlight the sinusoidal trend of the signal. Even though some noise is superposed to the wave, it is possible to recover the original signal with a simple sinusoidal fit of the data.

The second possible solution is the difference between every trace and the first one, used as a reference trace. What we obtain is a sort of temporal derivative, that make the continuous component to decrease, while increasing the sinusoidal trend of the data, and so the peak of the Fourier transform. As we can see from

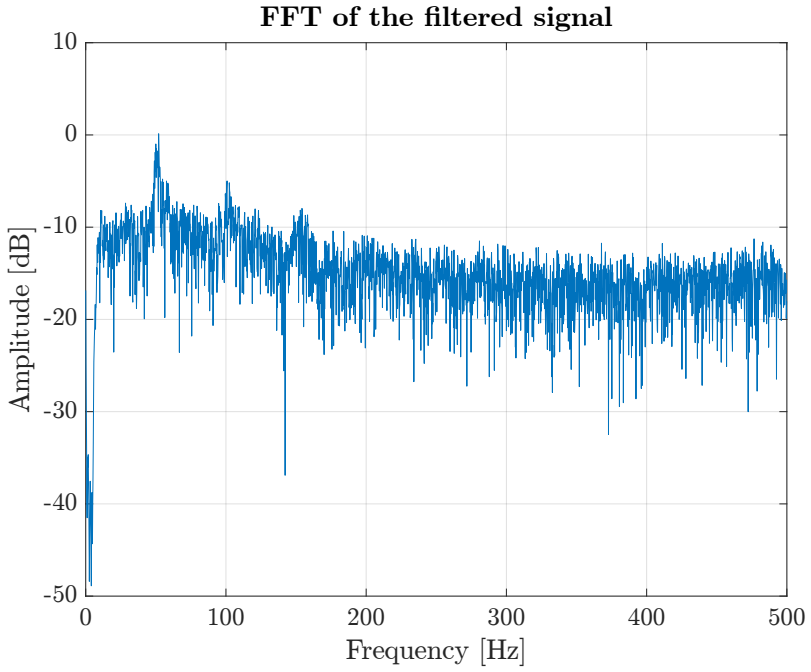

Figure 5.9: FFT of the filtered signal, averaged around the portion where the acoustic wave is applied.

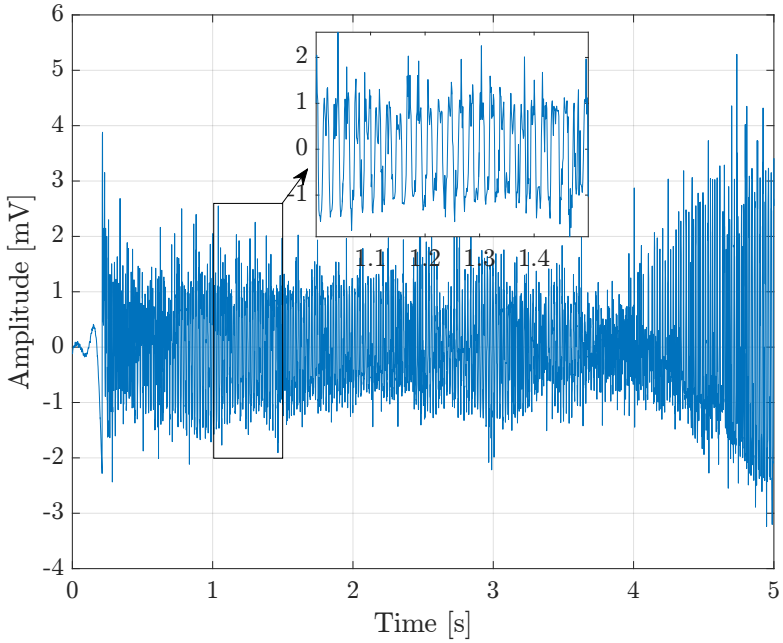

Figure 5.10: Time domain visualization of the signal around the perturbation.

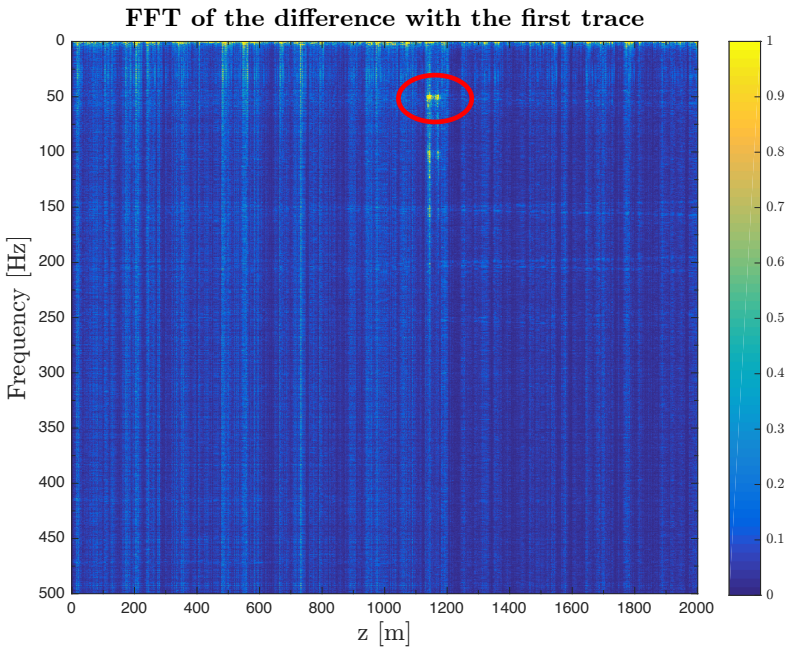

Figure 5.11: Spectrogram obtained by making the difference between each trace and the first one.

the spectrogram in Fig. 5.11 and the average value around the perturbation in Fig. 5.12, the improvements are not so appreciable with respect to the simple FFT (Fig. 5.4 and 5.6).

From the observation of the performed analysis, it is possible to state that the sinusoidal perturbation can be detected through a simple analysis of the traces in the frequency domain. The point of application can be found with an uncertainty of some meters, while working with a spatial resolution of 15 m. In particular, the perturbed portion of the fiber seems to be between 1130 and 1180 m while the actual application point is from 1140 to 1160 m. Also, the frequency of the acoustic wave can be detected quite accurately, as a peak of the absolute value of the FFT. However, it is not a single spectral line, but it involves a small range of frequencies around the central one: our measurement is affected by some uncertainty.
On the other hand, we can perform more accurate data analysis, to obtain some

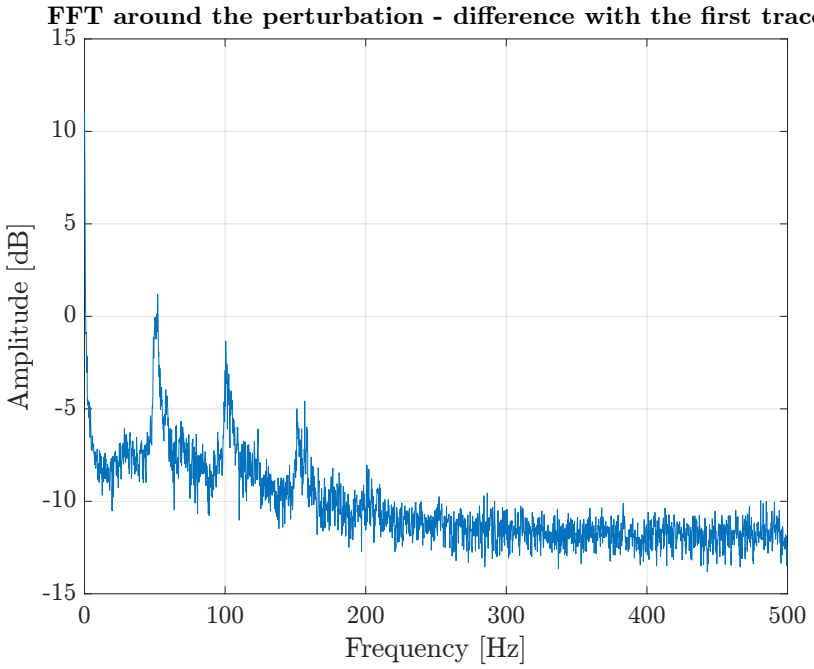

Figure 5.12: FFT obtained by making the difference between each trace and the first one around the perturbation.

improvements of the SNR level and to reduce the higher harmonic components. To this purpose, we have seen that the best results regarding trace SNR can be obtained in the case of normalization with respect to the average, and when the continuous component is filtered with a high pass filter.

After these first results for $f_a = 50$ Hz, the performances of our setup have been tested with higher frequencies, up to $f_a = 500$ Hz.
The tests have shown that it is always possible to detect the acoustic wave, with about the same uncertainty of some Hz and some meters we have seen in the case $f_a = 50$ Hz. However, before starting the acquisitions, it is always necessary to check the noise level with the power meter and to change the pulse amplitude whenever it is required. Otherwise, a too high noise level would affect the measurements, and the vibration detection would not be possible.

The following figures represent the results obtained for $f_a = 400$ Hz. The data analysis has been performed as in the case of $f_a = 50$ Hz.
From in Fig. 5.14 - 5.15 we can notice a small shift in frequency: the peak is not exactly centered at $f = 400$ Hz. This inaccuracy can be caused by different factors: the acquisition rate of the board is not exactly 1 kHz, hence the frequencies are not perfectly aligned when computing the Fourier transform, or the loudspeaker introduces some inaccuracy when amplifying the acoustic wave.
Moreover, the sinusoidal shape of the filtered signal (5.16) in the time domain is not so clear from the graph, due to the low sampling rate compared to the sinusoid period.
However, we can state that the perturbation has been correctly detected also in this case.

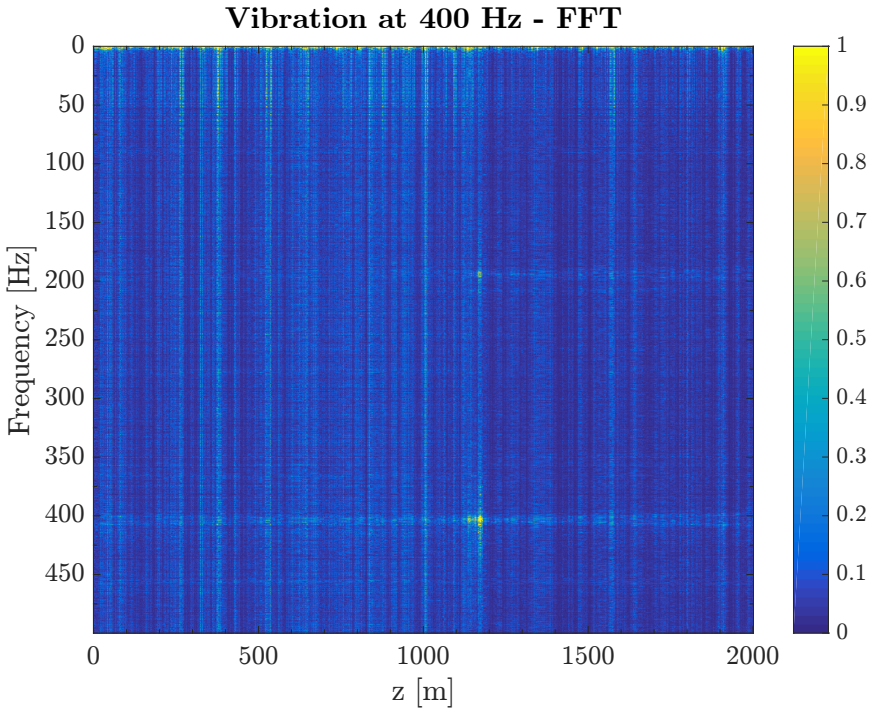

Figure 5.13: Spectrogram of the traces when a perturbation with $f_a = 400$ Hz is applied.

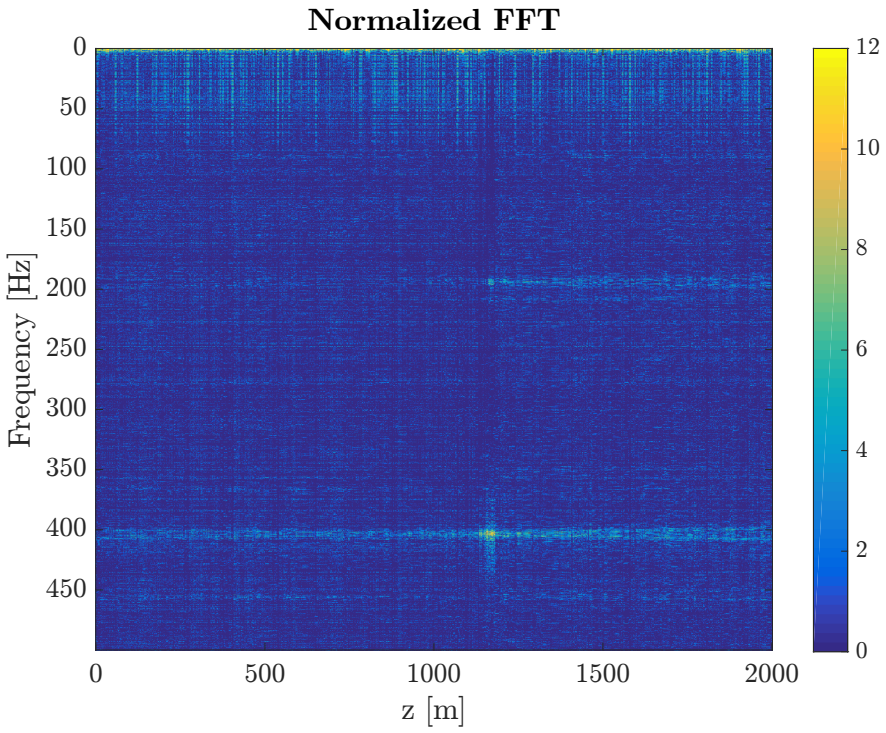

Figure 5.14: Normalized spectrogram with respect to the average value when a perturbation with $f_a = 400$ Hz is applied.

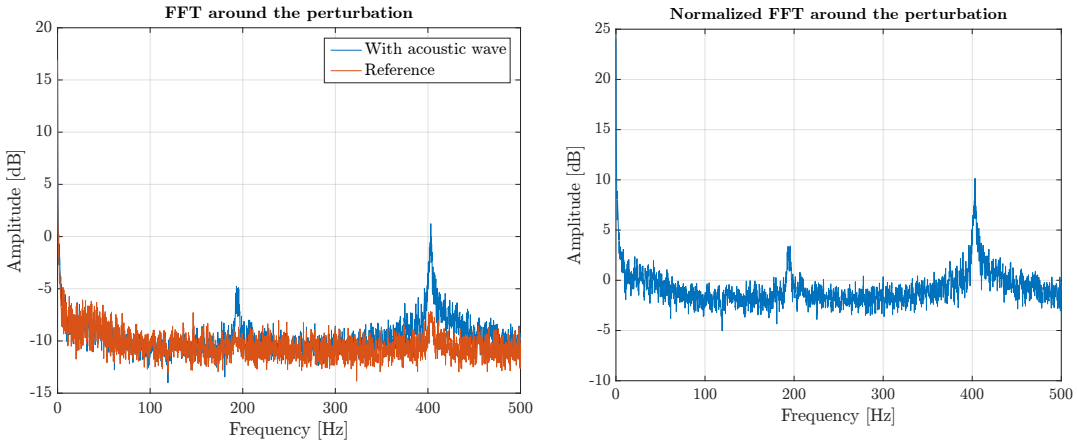

(a) (b)

Figure 5.15: FFT around the portion of the fiber where the acoustic wave is applied: comparison between the reference signal and the simple FFT (5.15a) and normalized FFT (5.16b).

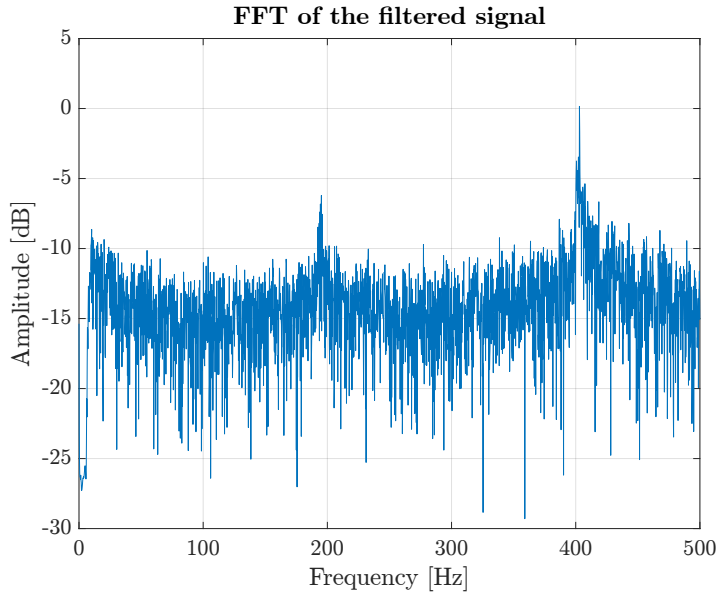

(a)

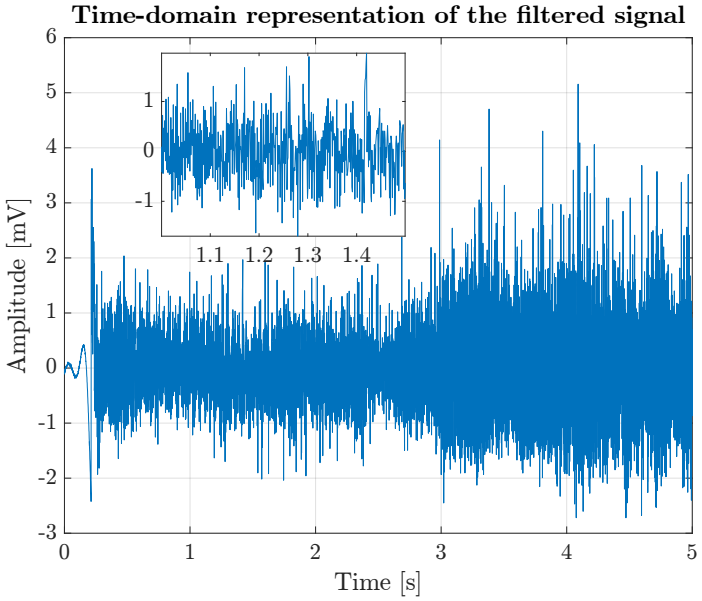

(b)

Figure 5.16: Signal filtered with a high-pass filter: FFT around the perturbed portion (5.16a) and time-domain visualization (5.16b) with a zoom for $t \in [1, 1.5]$ s.

6
Conclusions

In this thesis, we have designed a distributed acoustic sensor with the ϕ-OTDR technique. As a first step, the ϕ-OTDR setup has been implemented. One of the main components is the high coherence laser, which is necessary to develop a phase-sensitive OTDR. After having been modulated and amplified, the light is sent into the fiber coils, whose backscattering is detected by a photodiode and converted into an electric signal. The trace can be visualized with an oscilloscope.
A first version of the setup showed that the noise affecting the trace can increase with time, and is hugely dependent on the pulse amplitude. For this reason, we have introduced a power splitter after the modulator, allowing us to check the noise level, so that we can change the pulse amplitude whenever it is necessary.
Then, the traces have been acquired through a PCI acquisition board, the Signatec PDA14. We have written a new acquisition method, based on the principal acquisition mode of the board, to record a large number of traces continuously.
To test the performances of the ϕ-OTDR as a distributed acoustic sensor, we have applied different acoustic waves on a portion of the fiber through a loudspeaker, which amplified the sinusoidal signal generated by a function generator.
The tests have been made for different frequencies of the sinusoidal waves, from 50 Hz to 500 Hz. 500 Hz is the maximum frequency that can be detected with this setup, due to the limited acquisition frequency allowed by the computer (1 kHz).

The experimental results show that it is possible to correctly detect the acoustic wave frequency and the position along the fiber where it is applied.
However, the results should be improved in precision: in some cases, the detected frequency is a bit shifted with respect to the central one, in particular when it is close to the maximum detectable frequency. Moreover, the acoustic wave affects a portion of the fiber which is larger than the actual part that undergoes the perturbation.
These improvements may be obtained both with an improvement of the acquisition methods and with some changes in the setup. In the first case, a computer and acquisition board with higher performances would increase the acquisition rate. On the other hand, as it has been shown in many works, different methods allow obtaining more precise results and higher spatial resolution.
A first simple setup improvement may be the use of a polarization beam splitter and two photodiodes. Thus, two different signals would be acquire, referring to different polarization, and their sum would cancel some fluctuations and improve the SNR.
Therefore, two other techniques would allow to improve the results and the spatial resolution: the interferometric technique, and the use of chirped pulses.

References

[1] [Online]. Available: http://www.cablinginstall.com/articles/print/volume-25/issue-7/features/design/distributed-sensing-cable-in-industrial-environments.html

[2] X. Bao and L. Chen, "Recent progress in distributed fiber optic sensors," *Sensors*, no. 12, pp. 8601–8639, 2012.

[3] Y. Wang, B. Jin, Y. Wang, D. Wang, X. Liu, and Q. Bai, "Real-time distributed vibration monitoring system using ϕ- otdr," *IEEE Sensors Journal*, vol. 17, no. 5, pp. 1333–1341, 2017.

[4] I. Signatec, *PDA14 Operator's Manual*, Corona, California, USA, 2005.

[5] A. Barrias, J. R. Casas, and S. Villalba, "A review of distributed optical fiber sensors for civil engineering applications," *Sensors*, vol. 16, 2016.

[6] L. Palmieri and L. Schenato, "Distributed optical fiber sensing based on rayleigh scattering," *The Open Optics Journal*, vol. 7, pp. 104–127, 2013.

[7] C. G. Someda, *Electromagnetic Waves*. CRC Press - Taylor and Francis Group, 2006.

[8] S. Adachi, "Distributed optical fiber sensors and their applications," in *SICE Annual Conference*, August 2008.

[9] N. Takahashi, K. Tetsumura, K. Imamura, and S. Takahashi, "Underwater acoustic sensor with fiber bragg gratic," *Opt. Rev.*, vol. 4, no. 6, pp. 691–694, 1997.

[10] N. Takahashi, K. Yoshimura, and S. Takahashi, "Fiber bragg grating vibration sensor using incoherent light," *Jpn. J. Allp. Phys.*, vol. 40, no. 5b, pp. 1–6, 2001.

[11] N. Takahashi, K. Tetsumura, and K. Imamura, "Fbg vibration sensor based on intensity-modulation method with incoherent light," *Proc SPIE*, vol. 4416, pp. 62–65, 2001.

[12] I. Perez, H. L. Cui, and E. Udd, "High frequency ultrasonic wave detection using fiber bragg gratings," in *SPIE 7th Annu. Int. Symp. Smart Struct. Mater*, 2000.

[13] I. Perez, H. Cui, and E. Udd, "Acoustic emission detection using fiber bragg gratings," in *Proc. SPIE*, vol. 4328, 2001, pp. 209–215.

[14] A. Fernandez, P. Rodeghiero, B. Brichard, F. Berghmans, A. Hartog, P. Hughes, K. Williams, and A. Leach, "Radiation-tolerant raman distributed temperature monitoring system for large nuclear infrastructures." *IEEE Trans. Nucl. Sci.*, no. 52, pp. 2689–2694, 2005.

[15] K. Suh and C. Lee, "Auto-correction method for differential attenuation in a fiber-optic distributed-temperature sensor." *Opt. Lett.*, no. 33, pp. 1845–1847, 2008.

[16] M. Tanner, S. Dyer, B. Baek, R. Hadfield, and S. Woo Nam, "High-resolution single-mode fiber-optic distributed raman sensor for absolute temperature measurement using superconducting nanowire single-photon detectors," *Appl. Phys. Lett*, 2011.

[17] J. Park, G. Bolognini, D. Lee, P. Kim, P. Cho, F. di Pasquale, and N. Park, "Raman-based distributed temperature sensor with simplex coding and link optimization." *IEEE Photonics Technol. Lett.*, vol. 18, pp. 1879–1881, 2006.

[18] X. Bao, J. Dhliwayo, N. Heron, D. Webb, and D. Jackson, "Experimental and theoretical studies on a distributed temperature sensor based on brillouin scattering," *J. Lightwave Technol.*, vol. 13, pp. 1340–1348, 1995.

[19] T. Kurashima, T. Horiguchi, and M. Tateda, "Distributed-temperature sensing using stimulated brillouin scattering in optical silica fibers," *Opt. Lett.*, vol. 15, pp. 1038–1040, 1990.

[20] M. Nikles, L. Thevenaz, and P. Robert, "Simple distributed temperature sensor based on brillouin gain spectrum analysis," in *Proc. SPIE Int. Soc. Opt. Eng.*, 1994, pp. 138–141.

[21] K. Hotate and M. Tanaka, "Distributed fiber brillouin strain sensing with 1 cm spatial resolution by correlation-based continuous wave technique," *IEEE Photonics Technology Letters*, vol. 14, pp. 179–181, 2002.

[22] M. Belal and T. P. Newson, "A 5 cm spatial resolution temperature compensated distributed strain sensor evaluated using a temperature controlled strain rig." *Opt. Lett.*, vol. 36, pp. 4728–4730, 2011.

[23] L. Falco, P. Debergh, and T. Edye, "Bimorphous distributed transducer for the detection of temperature threshold," in *Anon, Ed. International Carnahan Conference on Security Technology*, IEEE, Ed., 1989.

[24] W. Michie, B. Culshaw, I. McKenzie, and al., "Distributed sensor for water and ph measurements using fiber optics and swellable polymeric systems," *Opt Lett*, vol. 20(1), pp. 103–105, 1995.

[25] J. Chai, S. Wei, X. Chang, and J. Liu, "Monitoring deformation and damage on rock structures with distributed fiber optical sensing," *Int J Rock Mech Mini Sci 2004*, vol. 41, pp. 298–303, 2004.

[26] K. Wanser and K. Voss, "Crack detection using multimode fiber optical time domain reflectometry," *Kersey Alan D DJP, editor. Proceedings of SPIE - The International Society for Optical Engi- neering.*, vol. 2294, pp. 43–52, 1994.

[27] X. Guangping, S. Leong Keey, and A. Asundi, "Optical time-domain reflectometry for distributed sensing of the structural strain and de- formation." *Opt Las Eng*, vol. 32(5), pp. 437–447, 1999.

[28] R. Lieberman, E. Mendoza, D. Ferrell, and al., "Intrinsic fiber optic sensor for distributed water detection," in *Proc. SPIE*, vol. 2068. Society of photo-optical instrumentation engineers, Bellingham., 1994, pp. 192–201.

[29] J. Buerck, S. Roth, K. Kraemer, and H. Mathieu, "Otdr fiber-optical chemical sensor system for detection and location of hydrocarbon leakage." *J. Hazard Mater*, vol. 102(1), pp. 13–28, 2003.

[30] A. Rogers, "Polarization-optical time domain reflectometry: a technique for the measurement of field distributions," *Appl Opt*, vol. 20, pp. 1060–1074, 1981.

[31] F. Corsi, A. Galtarossa, and L. Palmieri, "Polarization mode dispersion characterization of single-mode optical fiber using backscattering technique," *Lightwave Technol*, vol. 16(10), pp. 1832–1843, 1998.

[32] Y. Lu, T. Zhu, L. Chen, and X. Bao, "Distributed vibration sensor based on coherent detection of phase-otdr," *Journal of Lightwave Technology*, vol. 28, no. 22, pp. 3243–3249, 2010.

[33] J. C. Juarez, "Distributed fiber optic intrusion sensor system for monitoring long perimeters," Ph.D. dissertation, Texas A&M University, August 2005.

[34] J. Pastor-Graells, L. R. Cortés, M. R. Fernández-Ruiz, H. F. Martins, J. Azaña, S. Martin-Lopez, and M. Gonzalez-Herraez, "Snr enhancement in high-resolution phase-sensitive otdr systems using chirped pulse amplification concepts," *Opt. Lett.*, vol. 42, pp. 1728–1731, 2017.

[35] B. J. Soller, D. K. Gifford, M. S. Wolfe, and M. E. Froggatt, "High resolution optical frequency domain reflectometry for characterization of components and assemblies," *Optics Express*, vol. 12, no. 2, pp. 666–674, 2005.

[36] Y. Koshikiya, X. Fan, and F. Ito, "Highly sensitive coherent optical frequency-domain reflectometry employing ssb-modulator with cm-level spatial resolution over 5 km," in *Proceedings of the 33rd European Conference and Ehxibition of Optical Communication (ECOC)*, 2007.